Charles University in Prague
Faculty of Mathematics and Physics

MASTER THESIS

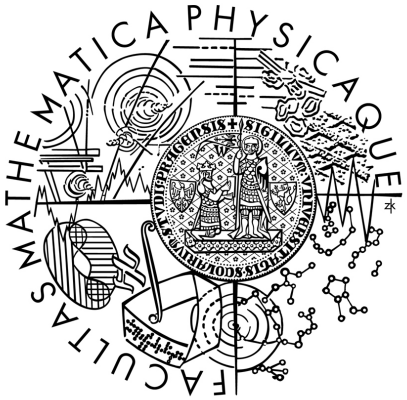

Petr Grinac

Seismic source modelling

Institute of Theoretical Physics

Supervisor: Doc. RNDr. Ctirad Matyska, DrSc.,
Department of Geophysics

Studying program: Mathematical and computer modelling in physics

2007

I would like to thank all people who supported me during my work on the thesis. I am especially indebted to my wise supervisor Ctirad Matyska, who had been very supportive. I'm grateful for geophysical consultations to Jan Burjánek and František Gallovič. At last I would like to thank my family and my beloved girlfriend Hanka for their patience and providing a tranquil surroundings during my work.

Prohlašuji, že jsem svou diplomovou práci napsal samostatně a výhradně s použitím citovaných pramenů. Souhlasím se zapůjčováním práce.

V Praze dne Petr Grinac

Contents

Název práce: Modelování seismického zdroje
Autor: Petr Grinac
Katedra (ústav): Ústav teoretické fyziky
Vedoucí diplomové práce: Doc. RNDr. Ctirad Matyska, DrSc.
e-mail vedoucího: cm@karel.mff.cuni.cz

Abstrakt: Práce se zabývá kinematickým popisem seismického zdroje v 3-D elastickém isotropním materiálu. K popisu používáme přiblížení malých deformací. Důraz je kladen na numerické metody, které vedou k získání přibližného řešení elastodynamických rovnic, tj. získat pole posunutí a napětí generovaná zdrojem. 3-D konečné prvky jsou základem prostorové diskretizace. Pozornost je soustředena na efekty, které přináší změny geometrie zdroje. Pro statický případ je řešení porovnáno s analytickým řešením. Pro časově závislé případy je řešení srovnáno s výsledky metody diskrétních vlnových čísel. Je studována závislost spekter oscilogramů na jemnosti prostorové diskretizace. Prezentovány jsou výsledky popisující závislost vlnového pole na geometrii pro po částech rovinný zlom.

Klíčová slova: kinematický seismický zdroj, konečné prvky, elastodynamika

Title: Seismic source modelling
Author: Petr Grinac
Department: Institute of Theoretical Physics
Supervisor: Doc. RNDr. Ctirad Matyska, DrSc.
Supervisor's e-mail address: cm@karel.mff.cuni.cz

Abstract: The work deals with a kinematic description of a seismic source in 3-D isotropic elastic medium. We use the concept of small deformations. Emphasis is on numerical approaches to obtain a solution of elastodynamic equations i.e. to obtain displacement and stress changes generated by the source. Spatial domain is discretized by the finite element method. Attention is focused on the effects due to changes of the source geometry. In the static case method is benchmarked against an analytic solution. Time dependent case is compared to results from the discrete wavenumber method. Spectra of seismograms are studied to investigate dependence of artificial oscillations on mesh coarseness. Dependence of results on source geometry is presented for piecewise planar fault surface.

Keywords: kinematic sesmic source, finite elements, elastodynamics, structural dynamics

Chapter 1

Introduction

Although it seems that the Earth remains static, it still continues evolving. The word static greatly depends on what time scale we choose to study particular phenomenon. If we watched mutual position of continents for hours, we would not find any time dependence. If watched for thousands of years, we would find that continents drift. Many processes connected with geology and geophysics are very slow and when describing them, we use time scale of years or longer. However, there are also very fast processes which take place in the Earth in time scale of seconds.

Earthquakes usually occur near active interfaces between lithospheric plates. In this work we recall a mathematical model which is based on continuum mechanics. Model employs linear elasticity to predict waves propagation from a seismic source. Source is represented by a time-dependent discontinuity in the displacement field. Space orientation and positioning of the fault zone is assumed to be known a priori. This work does not attempt to model actual rupturing processes that occur in real earthquakes. Seismic source is considered to be *kinematic*, which is a geophysical term for a priori prescribed discontinuity.

In the following two chapters we present a mathematical formulation of the problem in the framework of continuum mechanics. Problem is first formulated in standard form in the language of partial differential equations. This so called "strong" formulation is then used as a background for corresponding weak formulation, which is more convenient from mathematical point of view. Turning to weak formulation, we can establish existence and uniqueness for the solution of the problem.

The work's emphasis is laid on numerical approaches, which lead to approximate solution of the problem. Finite elements method is straightforwardly applied on the weak formulation to reduce infinite-dimensional problem into a finite set of linear ordinary differential equations. At this point

we introduce two methods for time-integration of resulting ODEs. Spatial discretization is done for three-dimensional computational domains. Three-dimensional approach fully describes fault zone geometry. Three-dimensional domains also have their difficulties. Main difficulty we have encountered was rapidly increasing number of degrees of freedom for resulting systems of equations.

Chapter 5 presents results obtained by previously introduced numerical methods. Static case is benchmarked against an analytic solution. Time evolving problems are compared to results obtained by the discrete wavenumber method. Certain difficulties are encountered while modeling formation of seismic waves. Approximate solutions exhibit presence of artificial oscillations, which have no physical background. Our computations suggest that these oscillations depend on coarseness of spatial discretization.

Whole motivation for this work was to find out, whether 3D linear finite elements method is a suitable numerical approach for seismological applications.

Chapter 2

Formulation of the problem

2.1 Governing equations

When one tries to describe physically certain phenomena, he usually has to focus on the dominant features and neglect those bringing only small effects. Later, when such a description is found to be insufficient one may add subtle features to improve the model. When we describe propagation of seismic waves through the Earth, we are going to simplify the situation too. The same holds for the description of the seismic source.

The first simplification comes when we choose the rheological model. We know, that soil exhibits effects like stress relaxation for example. Since wave propagation is a relatively fast process, it is sufficient to use only elasticity. Even if we used Maxwell rheology, it would not bring any new information, because effects based on stress relaxation would not have time to develop. Choice of pure elasticity also assures no damping for the propagating waves. There is always certain amount of damping involved in real seismic wave propagation. We assume that the amount of energy dissipation due to damping can be neglected. Our computation simulates displacement field only relatively close to rupture zone. This fact is caused by a rapidly rising computational effort in case of 3D finite elements, which limits the size of domain that can be used.

Propagation of seismic waves in elastic medium is described by the equation of motion in elastodynamics [12]. In addition, we will use isotropic case of the generalized Hook's law. Of course, material properties vary with position. For example volume density depends on depth. We will suppose that material properties are piecewise continuous functions of position. In numerical computation we will consider material properties to be constant in each element.

Radiation of energy is emitted by a mutual shift of opposing tectonic blocks along rupture zone. Observations from real earthquakes suggest that rupture thickness is very small compared to other dimensions of the fault. Therefore it is reasonable to approximate the rupture zone by a surface. The mutual shift of opposing media creates a discontinuity in the field of displacement. Our kinematic description of the seismic source will be represented as a time dependent displacement discontinuity along surface Γ. In other words, the discontinuity is prescribed a priori. Effort has been made to develop techniques of simulation and description of spontaneous rupture propagation, but this issue will not be considered here. Dynamic response of the elastic medium is described by the momentum equation

$$\rho \ddot{\boldsymbol{u}} - \nabla \cdot \boldsymbol{\tau} = \boldsymbol{f}, \tag{2.1.1}$$

where $\boldsymbol{u}$ denotes vector of displacement, $\boldsymbol{\tau}$ denotes the Cauchy stress tensor and $\boldsymbol{f}$ denotes volume forces density. Equation (2.1.1) holds for every $(\boldsymbol{x}, t) \in Q_T \equiv \Omega \times [0, T], \quad \boldsymbol{x} \in \mathbb{R}^3$. Two dots above a function denote second derivative with respect to time t.

Deformations that occur during the simulations are expected to be small. This assumption allows us to use the concept of *small deformations*, which greatly simplifies the treatment of the problem. The above mentioned isotropic Hook's law is given by

$$\boldsymbol{\tau} = \lambda(\nabla \cdot \boldsymbol{u})\boldsymbol{I} + 2\mu\boldsymbol{\varepsilon}(\boldsymbol{u}), \tag{2.1.2}$$

where $\boldsymbol{I}$ denotes the identity matrix and $\boldsymbol{\varepsilon}(\boldsymbol{u})$ denotes the tensor of small deformations. Tensor of small deformations is given as a symmetric part of displacement gradient

$$\boldsymbol{\varepsilon}(\boldsymbol{u}) = \frac{1}{2}\big(\nabla \boldsymbol{u} + \nabla \boldsymbol{u}^T\big). \tag{2.1.3}$$

Parameters λ, μ fully describe the behavior of an isotropic elastic medium. In the later discussion they will be referred to as Lame coefficients.

The region Ω represents a sufficiently large neighborhood of the source region. The top surface corresponds with the Earth's surface. There is a source fault Γ inside Ω. The fault surface represents the region where the displacements discontinuity occurs and is supposed to be buried inside Ω without any contact with other parts of the boundary.

The boundary of Ω consists of two parts Γ_D , Γ_N such that relation $\partial\Omega = \Gamma_D \cup \Gamma_N$ holds. The two dimensional measure of parts intersection is zero. One remark on notation - subscripts under boundary parts Γ_x refer to the type of prescribed boundary condition - Dirichlet or Neumann.

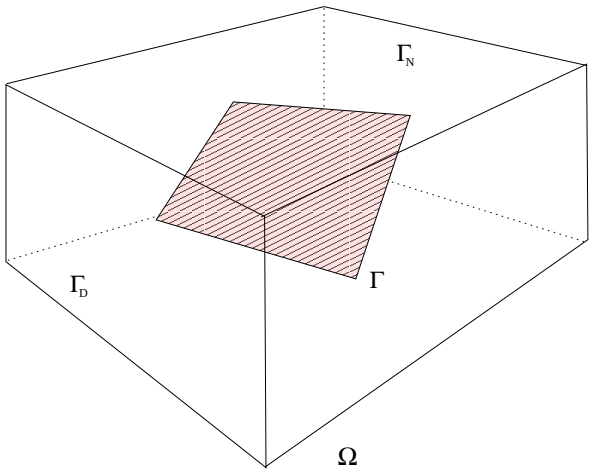

Figure 2.1: Region Ω. Fault surface Γ does not have a contact with other parts of boundary.

The following boundary conditions are prescribed:

$$\boldsymbol{u}(\boldsymbol{x},t) = 0 \qquad \forall(\boldsymbol{x},t) \in \Gamma_D \times [0,T], \tag{2.1.4a}$$

$$\boldsymbol{\tau}(\boldsymbol{x},t)\cdot\boldsymbol{n} = 0 \qquad \forall(\boldsymbol{x},t) \in \Gamma_N \times [0,T], \tag{2.1.4b}$$

where $\boldsymbol{n}$ denotes outer normal to Γ_N. The first condition assures zero displacements at the boundary. As soon as a wave reaches this boundary, it will be reflected. This reflection does not correspond with a real situation, where the wave would continue traveling. This fact must be taken into account when we choose time interval of computation. The second condition corresponds with the fact that we would like to describe a free surface of the Earth. It means that there are no forces acting on the surface.

On a buried fault Γ we assume that normal stress component is continuous. Next, along the fault we allow only shear-like slips. This means that the only direction of displacement discontinuity allowed across Γ is tangent to the surface. This condition also ensures that material does not penetrate itself and that no empty space is created on the fault. The condition is expressed by the fact that components of displacement normal to Γ must be continuous. On the fault surface Γ we prescribe the following discontinuity:

$$[\boldsymbol{u}\cdot\boldsymbol{n}]^+_- = 0 \qquad \forall(\boldsymbol{x},t) \in \Gamma \times [0,T], \tag{2.1.5a}$$

$$[\boldsymbol{u} - (\boldsymbol{u}\cdot\boldsymbol{n})\boldsymbol{n}]^+_- = \boldsymbol{f}_\Gamma(\boldsymbol{x},t) \qquad \forall(\boldsymbol{x},t) \in \Gamma \times [0,T], \tag{2.1.5b}$$

$$[\boldsymbol{\tau}\cdot\boldsymbol{n}]^+_- = 0 \qquad \forall(\boldsymbol{x},t) \in \Gamma \times [0,T], \tag{2.1.5c}$$

where $[...]^+_-$ denotes discontinuity across the surface Γ, or by other words the

difference of the quantity on opposite sides of Γ and $\boldsymbol{n}$ is the normal vector to surface Γ.

The above formulation of the problem is similar to formulations in another fields of physics, namely mechanics. Concept of slip, discontinuity in displacement field, is used to model dislocations in solids. Quite interesting method which was applied to similar problems with slips is called extended finite elements. This method is based on finite elements, but possesses one advantage over standard FEM: mesh on which the problem is computed does not have to respect discontinuities. Set of basis functions of the discrete space is "enriched" with discontinuous functions that capture slip properties. In the standard finite elements which are to be used here, element edges have to be aligned with the crack surface.

Chapter 3

Weak formulation of the problem

In order to get the existence and uniqueness of a solution it is preferable to formulate the studied problem in weak sense. Weak formulation naturally offers a way to discretize the problem by the finite elements method.

3.1 Motivation for definition of weak formulation

Assume $\boldsymbol{u}$ is a smooth solution of equation (2.1.1) satisfying boundary conditions discussed in the previous chapter. By the word smooth we mean that $\boldsymbol{u} \in C^2(\overline{\Omega} \setminus \Gamma; \mathbb{R}^3)$. Note, that $\boldsymbol{u}$ possesses a discontinuity across Γ.

Define $\mathcal{V} \equiv \{\boldsymbol{v} \in C^\infty(\Omega; \mathbb{R}^3) : \boldsymbol{v} \mid_{\Gamma_D} = 0\}$. Let $\boldsymbol{v} \in \mathcal{V} \cap C^1(\overline{\Omega}; \mathbb{R}^3)$. Make a scalar product of equation (2.1.1) with function $\boldsymbol{v} \in \mathcal{V} \cap C^1(\overline{\Omega}; \mathbb{R}^3)$ and integrate over region Ω to get

$$\int_\Omega \rho \ddot{\boldsymbol{u}} \cdot \boldsymbol{v} \, \mathrm{d}x - \int_\Omega (\nabla \cdot \boldsymbol{\tau}) \cdot \boldsymbol{v} \, \mathrm{d}x = \int_\Omega \boldsymbol{f} \cdot \boldsymbol{v} \, \mathrm{d}x \quad \boldsymbol{v} \in \mathcal{V} \cap C^1(\overline{\Omega}; \mathbb{R}^3). \quad (3.1.1)$$

Suppose that density and Lame coefficients are $\rho, \lambda, \mu \in L^\infty(\Omega)$. We will split the region Ω into two regions Ω_Γ and $\Omega_\Gamma^C = \Omega \setminus \overline{\Omega}_\Gamma$. Boundary of Ω_Γ consists of the fault surface Γ and the rest, which will be denoted $\Theta = \partial\Omega_\Gamma \setminus \overline{\Gamma}$. We suppose that region Ω_Γ has a positive measure and that it has a Lipchitz boundary. Figure 3.1 shows how such a region could look like. Region Ω_Γ is supposed to occupy only one side of the fault surface Γ. After we have introduced two regions Ω_Γ and Ω_Γ^C we can write

$$\int_\Omega \rho \ddot{\boldsymbol{u}} \cdot \boldsymbol{v} \, \mathrm{d}x - \int_{\Omega_\Gamma} (\nabla \cdot \boldsymbol{\tau}) \cdot \boldsymbol{v} \, \mathrm{d}x - \int_{\Omega_\Gamma^C} (\nabla \cdot \boldsymbol{\tau}) \cdot \boldsymbol{v} \, \mathrm{d}x = \int_\Omega \boldsymbol{f} \cdot \boldsymbol{v} \, \mathrm{d}x. \quad (3.1.2)$$

We will split the solution $\boldsymbol{u}$ into two parts $\tilde{\boldsymbol{u}}$ and $\boldsymbol{u}_\Gamma$, while relation

$$\boldsymbol{u} = \begin{cases} \tilde{\boldsymbol{u}} & \text{for } \boldsymbol{x} \in \Omega_\Gamma^C, \\ \tilde{\boldsymbol{u}} + \boldsymbol{u}_\Gamma & \text{for } \boldsymbol{x} \in \Omega_\Gamma \end{cases} \tag{3.1.3}$$

holds. The idea is that the the function $\tilde{\boldsymbol{u}}$ is continuous across Γ and the discontinuity is created by addition of function $\boldsymbol{u}_\Gamma$ which is known. We assume $\boldsymbol{u}_\Gamma$ has certain properties in order to make this decomposition meaningful. We assume that:

- $supp(\boldsymbol{u}_\Gamma) \subset \Omega_\Gamma$,
- $\boldsymbol{u}_\Gamma|_\Gamma = \boldsymbol{f}_\Gamma \qquad$ for all $0 \leq t \leq T$,
- $\boldsymbol{u}_\Gamma|_\Theta = 0 \qquad$ for all $0 \leq t \leq T$.

For reasons which will become apparent later, we will demand a little bit more, than the last condition. We want the function $\boldsymbol{u}_\Gamma$ to be zero not only directly on the boundary part Θ, but in a certain finite neighborhood of Θ. The reason is that we need also its spatial derivatives to have a zero trace on Θ. This demand does not restrict a class of functions which possess such a property, because we can simply broaden the region Ω_Γ beyond the part of boundary Θ and redefine function $\boldsymbol{u}_\Gamma$ by zero on the added region.

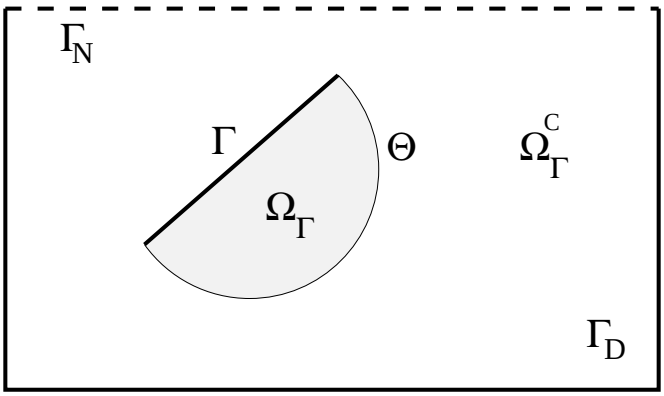

Figure 3.1: Slice through region Ω. Particular shape of Ω_Γ does not play a significant role, because solution does not depend on choice of extension $\boldsymbol{u}_\Gamma$.

We will now discuss only integrals over Ω_Γ and Ω_Γ^C in equation (3.1.2). Apply Green's theorem on the first integral over Ω_Γ to get

$$\int_{\Omega_\Gamma} (\nabla \cdot \boldsymbol{\tau}) \cdot \boldsymbol{v} \, \mathrm{d}x = \int_{\Gamma \cup \Theta} \boldsymbol{\tau} \cdot \boldsymbol{n} \cdot \boldsymbol{v} \, \mathrm{d}S - \int_{\Omega_\Gamma} \boldsymbol{\tau} : \boldsymbol{\varepsilon}(\boldsymbol{v}) \, \mathrm{d}x. \tag{3.1.4}$$

The same procedure done on the second integral gives

$$\int_{\Omega_\Gamma^C} (\nabla \cdot \boldsymbol{\tau}) \cdot \boldsymbol{v} \, \mathrm{d}x = \int_{\Gamma \cup \Theta \cup \Gamma_D \cup \Gamma_N} \boldsymbol{\tau} \cdot \boldsymbol{n} \cdot \boldsymbol{v} \, \mathrm{d}S - \int_{\Omega_\Gamma^C} \boldsymbol{\tau} : \boldsymbol{\varepsilon}(\boldsymbol{v}) \, \mathrm{d}x. \tag{3.1.5}$$

We have used the fact that the Cauchy stress tensor is symmetric and therefore $(\boldsymbol{\tau} \cdot \boldsymbol{v}) \cdot \boldsymbol{n} = (\boldsymbol{\tau} \cdot \boldsymbol{n}) \cdot \boldsymbol{v}$ holds. The surface integral over union of surfaces which have empty intersection can be written as a sum of integrals over each surface. Integral over Γ_D is equal to zero since $\boldsymbol{v} \in \mathcal{V}$ and therefore such a function is zero on Γ_D. Next, integral over Γ_N is also equal to zero because of the boundary condition for free surface (2.1.4b). Now we can see that the only integrals that now play a role are integrals over Γ and Θ. Please note that $\boldsymbol{n}$, which denotes outer normal, has an opposite sign for integrals in (3.1.4) and (3.1.5). Having this in mind, we can write

$$-\int_\Omega \nabla \cdot \boldsymbol{\tau} \cdot \boldsymbol{v} \, \mathrm{d}x = -\int_{\Gamma \cup \Theta} [(\boldsymbol{\tau} \cdot \boldsymbol{n}) \cdot \boldsymbol{v}]_-^+ \, \mathrm{d}S + \int_\Omega \boldsymbol{\tau} : \boldsymbol{\varepsilon}(\boldsymbol{v}) \, \mathrm{d}x. \tag{3.1.6}$$

Symbol $[...]_-^+$ denotes a difference of the quantity on opposite sides of the surface where it is evaluated. Stress tensor is a linear function of displacement, so $\boldsymbol{\tau}(\boldsymbol{u}) = \boldsymbol{\tau}(\tilde{\boldsymbol{u}}) + \boldsymbol{\tau}(\boldsymbol{u}_\Gamma)$. Putting this into equation (3.1.2) and incorporating the above discussion of surface integrals yields

$$\begin{aligned} \int_\Omega \rho \ddot{\tilde{\boldsymbol{u}}} \cdot \boldsymbol{v} \, \mathrm{d}x + \int_\Omega \boldsymbol{\tau}(\tilde{\boldsymbol{u}}) : \boldsymbol{\varepsilon}(\boldsymbol{v}) \, \mathrm{d}x = \int_\Omega \boldsymbol{f} \cdot \boldsymbol{v} \, \mathrm{d}x - \int_{\Omega_\Gamma} \rho \ddot{\boldsymbol{u}}_\Gamma \cdot \boldsymbol{v} \, \mathrm{d}x \\ - \int_{\Omega_\Gamma} \boldsymbol{\tau}(\boldsymbol{u}_\Gamma) : \boldsymbol{\varepsilon}(\boldsymbol{v}) \, \mathrm{d}x + \int_{\Gamma \cup \Theta} [(\boldsymbol{\tau}(\boldsymbol{u}) \cdot \boldsymbol{n}) \cdot \boldsymbol{v}]_-^+ \, \mathrm{d}S. \end{aligned} \tag{3.1.7}$$

Since we have assumed that $\tilde{\boldsymbol{u}}$ was $C^2(\Omega; \mathbb{R}^3)$, it follows that $\int_S [(\boldsymbol{\tau}(\tilde{\boldsymbol{u}}) \cdot \boldsymbol{n}) \cdot \boldsymbol{v}]_-^+ \, \mathrm{d}S = 0$ for any surface S inside Ω. If we take a closer look at the surface integral in equation (3.1.7) we will see that

$$\int_{\Gamma \cup \Theta} [(\boldsymbol{\tau}(\boldsymbol{u}) \cdot \boldsymbol{n}) \cdot \boldsymbol{v}]_-^+ \, \mathrm{d}S = \int_\Gamma [(\boldsymbol{\tau}(\boldsymbol{u}) \cdot \boldsymbol{n}) \cdot \boldsymbol{v}]_-^+ \, \mathrm{d}S + \int_\Theta [(\boldsymbol{\tau}(\tilde{\boldsymbol{u}}) \cdot \boldsymbol{n}) \cdot \boldsymbol{v}]_-^+ \, \mathrm{d}S, \tag{3.1.8}$$

because we assumed that $\boldsymbol{\tau}(\boldsymbol{u}_\Gamma)|_\Theta = 0$. Recall boundary condition (2.1.5c) to see that the integral over Γ must be zero. Smoothness of $\tilde{\boldsymbol{u}}$ ensures that the second integral over Θ is zero too. We can see now that no surface integrals play a role in weak formulation of the problem.

Putting all the above statements together we arrive at identity

$$\begin{aligned} \int_\Omega \rho \ddot{\tilde{\boldsymbol{u}}} \cdot \boldsymbol{v} \, \mathrm{d}x + \int_\Omega \boldsymbol{\tau}(\tilde{\boldsymbol{u}}) : \boldsymbol{\varepsilon}(\boldsymbol{v}) \, \mathrm{d}x = \int_\Omega \boldsymbol{f} \cdot \boldsymbol{v} \, \mathrm{d}x - \\ \int_{\Omega_\Gamma} \rho \ddot{\boldsymbol{u}}_\Gamma \cdot \boldsymbol{v} \, \mathrm{d}x - \int_{\Omega_\Gamma} \boldsymbol{\tau}(\boldsymbol{u}_\Gamma) : \boldsymbol{\varepsilon}(\boldsymbol{v}) \, \mathrm{d}x \quad \boldsymbol{v} \in \mathcal{V} \cap C^1(\overline{\Omega}; \mathbb{R}^3). \end{aligned} \tag{3.1.9}$$

3.2 Definition of weak solution

Natural choice for the space of test functions is Sobolev space $W^{1,2}(\Omega;\mathbb{R}^3)$ with zero traces on Γ_D.

Definition 3.2.1. *We will denote by V the space of test functions.*

$$V \equiv \{\boldsymbol{v} \in W^{1,2}(\Omega;\mathbb{R}^3) : \boldsymbol{v}|_{\Gamma_D} = 0\} \tag{3.2.1}$$

Traces of functions $\boldsymbol{v}$ are considered in the sense of trace theorem - see appendix A.0.1.

To simplify notation we will introduce a bilinear operator which will represent the integral containing stress tensor.

Definition 3.2.2. *Let $\boldsymbol{u}, \boldsymbol{v} \in W^{1,2}(\Omega;\mathbb{R}^3)$. Then we define a bilinear form $A : W^{1,2}(\Omega;\mathbb{R}^3) \times W^{1,2}(\Omega;\mathbb{R}^3) \longrightarrow \mathbb{R}$ by formula*

$$A(\boldsymbol{u}, \boldsymbol{v}) := \int_\Omega \lambda(\nabla \cdot \boldsymbol{u})(\nabla \cdot \boldsymbol{v}) + 2\mu\boldsymbol{\varepsilon}(\boldsymbol{u}) : \boldsymbol{\varepsilon}(\boldsymbol{v}) \, \mathrm{d}x. \tag{3.2.2}$$

We can slightly weaken our assumptions on the extension $\boldsymbol{u}_\Gamma$ of discontinuity function $\boldsymbol{f}_\Gamma$. Let $\boldsymbol{f}_\Gamma$ be such, that there exists $\boldsymbol{u}_\Gamma \in L^2\left(0,T;W^{1,2}(\Omega_\Gamma;\mathbb{R}^3)\right)$, with $\dot{\boldsymbol{u}}_\Gamma \in L^2\left(0,T;L^2(\Omega_\Gamma;\mathbb{R}^3)\right)$ and $\ddot{\boldsymbol{u}}_\Gamma \in L^2\left(0,T;L^2(\Omega_\Gamma;\mathbb{R}^3)\right)$ with properties already mentioned when we showed motivation for definition of weak solution.

Integral identity which we arrived at after assuming that $\boldsymbol{u}$ is a smooth solution of the problem has a well defined meaning for functions from more general spaces. Using definition of our bilinear operator $A(.,.)$ we can rewrite equation (3.1.9) for test functions in V:

$$(\ddot{\tilde{\boldsymbol{u}}}, \rho\boldsymbol{v}) + A(\tilde{\boldsymbol{u}}, \boldsymbol{v}) = (\boldsymbol{f}, \boldsymbol{v}) - (\ddot{\boldsymbol{u}}_\Gamma, \rho\boldsymbol{v}) - A(\boldsymbol{u}_\Gamma, \boldsymbol{v}) \quad \boldsymbol{v} \in V. \tag{3.2.3}$$

Scalar product in the space $L^2(\Omega;\mathbb{R}^3)$ is denoted by $(.,.)$. Please accept that if function $\boldsymbol{u}_\Gamma$ appears as a argument of scalar product or operator $A(.,.)$ we integrate only over Ω_Γ. We use this convention also in the following definition of weak solution.

Definition 3.2.3. *Let $\tilde{\boldsymbol{u}} \in L^2(0,T;V)$, $\dot{\tilde{\boldsymbol{u}}} \in L^2(0,T;L^2(\Omega;\mathbb{R}^3))$ and $\ddot{\tilde{\boldsymbol{u}}} \in L^2(0,T;V')$. Let $\boldsymbol{u}_\Gamma$ satisfy the above assumptions. Then $\boldsymbol{u} = \tilde{\boldsymbol{u}} + \boldsymbol{u}_\Gamma$ is a weak solution of our problem provided*

- $\langle\ddot{\tilde{\boldsymbol{u}}}, \rho\boldsymbol{v}\rangle + A(\tilde{\boldsymbol{u}}, \boldsymbol{v}) = (\boldsymbol{f}, \boldsymbol{v}) - (\ddot{\boldsymbol{u}}_\Gamma, \rho\boldsymbol{v}) - A(\boldsymbol{u}_\Gamma, \boldsymbol{v}) \qquad \forall \boldsymbol{v} \in V$ *and a.e.* $0 \leq t \leq T$.

- $\tilde{\boldsymbol{u}}(0) = \mathbf{g} \quad and \quad \dot{\tilde{\boldsymbol{u}}}(0) = \mathbf{h}$

where $g \in W^{1,2}(\Omega; \mathbb{R}^3), \quad h \in L^2(\Omega; \mathbb{R}^3)$.

Let us remark that if a function $\tilde{\boldsymbol{u}} \in L^2(0,T;V)$ satisfies the assumptions of definition (3.2.3), it is also continuously differentiable in time. Then conditions on an initial state have a well defined meaning. The theorem can be found in [10, pg. 286]. Energy estimates furthermore show, that $\tilde{\boldsymbol{u}} \in L^\infty(0,T;V)$ with $\dot{\tilde{\boldsymbol{u}}} \in L^\infty(0,T;L^2(\Omega;\mathbb{R}^3))$ and $\ddot{\tilde{\boldsymbol{u}}} \in L^2(0,T;V')$.

3.3 Sketch of proof of existence and uniqueness

We would like to recall definition of V-ellipticity for bilinear operators: we say that a bilinear operator $A : V \times V \to \mathbb{R}$ is V-elliptic if there exists a constant C such that

$$A(\boldsymbol{v}, \boldsymbol{v}) \geq C \, ||\boldsymbol{v}||_V \tag{3.3.1}$$

holds for every $\boldsymbol{v} \in V$. If we want to establish V-ellipticity of operator $A(.,.)$, we have to demand certain properties of Lame coefficient to hold.

Lemma 3.3.1. *Assume* $\lambda, \mu \in L^\infty(\Omega)$. *Furthermore assume that* $\lambda(\boldsymbol{x}) \geq 0$, $\mu(\boldsymbol{x}) \geq \mu_0 > 0 \quad$ *for a.e.* $\boldsymbol{x} \in \Omega$. *Then operator* $A(.,.)$ *is V-elliptic.*

Proof. $\int_\Omega \lambda(\nabla \cdot \boldsymbol{v})(\nabla \cdot \boldsymbol{v}) + 2\mu\boldsymbol{\varepsilon}(\boldsymbol{v}) : \boldsymbol{\varepsilon}(\boldsymbol{v}) \, \mathrm{d}x \geq 2\mu_0 \int_\Omega \boldsymbol{\varepsilon}(\boldsymbol{v}) : \boldsymbol{\varepsilon}(\boldsymbol{v}) \, \mathrm{d}x$ and Korn's inequality (see appendix A.0.2) completes the proof. □

For static case proof of existence uses Lax-Milgam lemma. Lax-Milgram lemma assumes that the left hand side bilinear operator is bounded and V-elliptic. Applying Lax-Milgram gives existence and uniqueness. Property of V-ellipticity also ensures that the matrix based on this operator on a discrete space V_h is positive definite.

Proof of existence and uniqueness for hyperbolic evolution problem with scalar unknown is thoroughly discussed in Evans [10, pg. 380-387]. This proof for scalar case can be easily adapted to accommodate our particular setting. Already adapted proof can be found in [15].

From uniqueness of a solution of the problem it can be shown that the sum of $\tilde{\boldsymbol{u}} + \boldsymbol{u}_\Gamma$ does not depend on particular choice of the extension $\boldsymbol{u}_\Gamma$. Particular shape of region Ω_Γ is also arbitrary within already mentioned properties that we demanded from it.

Chapter 4

Numerical approximation

Weak formulation of the problem is very useful when one wants to acquire an approximate solution. In this chapter we will discretize the infinite dimensional problem with the method of finite elements to get a system of ordinary differential equations. The system of ODEs is then integrated using two different schemes. For the upcoming discussion let us assume that Ω is a polygonal region with a Lipschitz boundary.

4.1 Finite elements - P^1 approximation

First let us introduce finite dimensional space V_h which approximates the space V. Let T_h be a triangulation of the region Ω with the properties:

- $\bigcup_{K \in T_h} = \Omega$
- if $K_i \cap K_j \neq \emptyset$, $i \neq j$ then either $K_i \cap K_j$ is a point or a whole edge or a whole face of the element.

Definition 4.1.1. *We will denote by V_h the space of piecewise linear continuous functions on the region Ω:*

$$V_h \equiv \{\boldsymbol{v} \in V : \boldsymbol{v}|_K \in P^1(K) \text{ for every } K \in T_h\}, \tag{4.1.1}$$

where $P^1(K)$ is the space of all polynomials defined on the region K of order less or equal to one.

Let $\{\boldsymbol{v}_i\}_{i=1}^{DOF}$ be a basis of the space V_h. Then every vector $\boldsymbol{v} \in V_h$ can be decomposed into the basis: $\boldsymbol{v} = \sum_i \boldsymbol{c}_i \boldsymbol{v}_i$. In the discrete formulation, our bilinear operators are going to adopt form of matrices. Similarly, linear form will appear as vector.

Definition 4.1.2. *Operators appearing in the definition of weak solution are thanks to basis in finite-dimensional space V_h represented as matrices or vectors*

$$A_{ij} := A_h(\boldsymbol{v}_j, \boldsymbol{v}_i), \tag{4.1.2}$$
$$D_{ij} := (\rho \boldsymbol{v}_i, \boldsymbol{v}_j)_h, \tag{4.1.3}$$
$$F_i := (\boldsymbol{f}, \boldsymbol{v}_i)_h. \tag{4.1.4}$$

Subscript h indicates a form of operators, where numeric quadrature rules are used to compute the integrals. Quadrature rules that were used will be discussed later.

The discrete problem formulated as a system of ordinary differential equations for coefficients $\boldsymbol{c}_i(t)$ adopts the form

$$\begin{aligned} D\ddot{\boldsymbol{c}}(t) + A\boldsymbol{c}(t) = F(t) \quad & t \in [0, T], \\ & \boldsymbol{c}(0) = \boldsymbol{g}, \\ & \dot{\boldsymbol{c}}(0) = \boldsymbol{h}, \end{aligned} \tag{4.1.5}$$

where $\boldsymbol{g}$, $\boldsymbol{h}$ denote the initial conditions for the system. Matrices A and D are usually reffered to as the stifness matrix and the mass matrix respectively.

According to standard theory of ordinary differential equations the system (4.1.5) has a unique C^2 solution.

4.2 Discretization of the time domain

As we have seen in the last section, space domain discretization by finite elements method leads to a system of ODEs for coefficients $\boldsymbol{c}_i$. The approximate solution is then obtained by making a linear combination of basis functions using these coefficients. There remains one question: How to solve the system of ODEs?

Let Δt be the time step. We will use the abbreviation for a function on i-th time level: $\boldsymbol{v}(t_i) = \boldsymbol{v}^i$ where $t_i = i\Delta t$. In following subsections we offer two methods for integration of the system. For the first scheme we will prove that the method exhibits a certain order of accuracy and that it is unconditionally stable. In order to show this, we need a notion of modal decomposition of the system (4.1.5).

4.2.1 Modal decomposition

Concept of modal decomposition was adopted from Zienkiewicz and Taylor [18]. Suppose we have a system of n linear differential equations of second

order in form

$$D\ddot{\boldsymbol{c}} + A\boldsymbol{c} = 0, \tag{4.2.1}$$

where D is the mass matrix and A is the stiffness matrix. For both matrices we suppose they are symmetric and positive definite. General solution of equation (4.2.1) can be written as

$$\boldsymbol{c} = \bar{\boldsymbol{c}} \exp(\mathrm{i}\omega t). \tag{4.2.2}$$

Feeding this into (4.2.1) we get

$$\left(-\omega^2 D + A\right) \bar{\boldsymbol{c}} = 0, \tag{4.2.3}$$

which is in fact the equation for eigenvalues ω_i^2 and eigenvectors $\bar{\boldsymbol{c}}_i$. Eigenvalues can be obtained by solving equation $\det(-\omega^2 D + A) = 0$. It is common in literature to fix uniqueness of eigenvectors by demanding that

$$\bar{\boldsymbol{c}}_i^T D \bar{\boldsymbol{c}}_i = 1 \tag{4.2.4}$$

holds for $i = 1...n$. Eigenvectors of this system have the important property of so called *modal orthogonality*. It can be shown [18] that the following holds:

$$\bar{\boldsymbol{c}}_i^T D \bar{\boldsymbol{c}}_j = 0 \quad \text{for} \quad i \neq j, \tag{4.2.5}$$

$$\bar{\boldsymbol{c}}_i^T A \bar{\boldsymbol{c}}_j = 0 \quad \text{for} \quad i \neq j. \tag{4.2.6}$$

This result was established under assumption that all eigenvalues ω_i are distinct. Furthermore relation

$$\bar{\boldsymbol{c}}_i^T A \bar{\boldsymbol{c}}_i = \omega_i^2 \tag{4.2.7}$$

is satisfied.

Let's consider (4.2.1) with a source term on the right-hand side

$$D\ddot{\boldsymbol{c}} + A\boldsymbol{c} = F. \tag{4.2.8}$$

If the equation (4.2.8) was homogeneous, general solution would have form[1] $\boldsymbol{c} = \sum_j \bar{\boldsymbol{c}}_j \exp(\mathrm{i}\omega_j t)$. For inhomogeneous case we will suppose the solution in form $\boldsymbol{c} = \sum_j \bar{\boldsymbol{c}}_j y_j(t)$. Feed this into equation (4.2.8) and make a scalar product of the result with $\bar{\boldsymbol{c}}_i$ to get

$$\bar{\boldsymbol{c}}_i^T D \sum_j \bar{\boldsymbol{c}}_j \ddot{y}_j + \bar{\boldsymbol{c}}_i^T A \sum_j \bar{\boldsymbol{c}}_j y_j = \bar{\boldsymbol{c}}_i^T F. \tag{4.2.9}$$

[1] Please be so kind and forgive us a little inconsistency in notation. Of course i means imaginary unit here.

Recalling earlier established *modal orthogonality*, equation (4.2.9) is reduced to a set of *scalar and uncoupled* equations for y_i

$$\ddot{y}_i + \omega_i^2 y_i = f_i. \tag{4.2.10}$$

We have used (4.2.7), (4.2.4), (4.2.5), (4.2.6). $f_i = \bar{\boldsymbol{c}}_i^T F$.

The main result of this subsection is that the system of ordinary differential equations (4.2.8) can be transformed into n scalar and *uncoupled* equations for coefficients y_i. This property happens to be very useful in analysis of stability of integration algorithms. Instead of analyzing the algorithm for a complicated system of equations, we can simply establish stability results for the corresponding scalar equation, where it is much easier.

4.2.2 Central difference, Crank-Nicolson like scheme

The first method for integration of the system (4.1.5) can be obtained as follows. We discretize the second derivative operator by a central difference term

$$\ddot{\boldsymbol{v}} \longrightarrow \frac{\boldsymbol{v}^{i+1} - 2\boldsymbol{v}^i + \boldsymbol{v}^{i-1}}{\Delta t^2}. \tag{4.2.11}$$

Then express the remaining terms by the mean value of functions on the following and past time level. Usage of a mean value resembles Crank-Nicolson scheme. We thus obtain scheme

$$D\frac{\boldsymbol{c}^{i+1} - 2\boldsymbol{c}^i + \boldsymbol{c}^{i-1}}{\Delta t^2} + A\frac{\boldsymbol{c}^{i+1} + \boldsymbol{c}^{i-1}}{2} = \frac{1}{2}\left(F^{i+1} + F^{i-1}\right). \tag{4.2.12}$$

The scheme is implicit. It will be shown that it provides unconditional stability regardless on the time step Δt and offers a second order accuracy.

To get the approximation on the next time level, one has to solve system of equations in form:

$$\left[A + \frac{2}{(\Delta t)^2}D\right]\boldsymbol{c}^{i+1} = F^{i+1} + F^{i-1} - A\boldsymbol{c}^{i-1} + \frac{4}{(\Delta t)^2}D(\boldsymbol{c}^i - 2\boldsymbol{c}^{i-1}). \tag{4.2.13}$$

As we shall see, the left-hand side operator that defines equation for $\boldsymbol{c}^{n+1}$ is a special case of an operator given by Bossak-Newmark method. System (4.2.13) has unique solution. Furthermore a sum of two positive definite operators appearing on the left-hand side is again a positive definite operator, so method of conjugate gradients can be used to solve the system. In the following discussion we show that the scheme is of second order a prove the stability result. In order to get this, we will review a few facts from the theory of linear multistep methods.

Review of the theory of linear multistep methods

General theory for multistep linear methods is well developed and summary of the theory can be found in [6]. The theory is formulated for systems of differential equations of form $\dot{y} = f(t, y)$. This case covers all situations, because any equation which involves higher order derivatives can be reduced to this form with simple transformation of variables. However for special case of second order equation of form $\ddot{y} = f(t, y)$ it is recommended to apply special theory developed for this case instead of reducing the equation to first order. Particular case of equation $\ddot{y} = f(t, y)$ is thoroughly discussed in [9]. The following paragraph follows this theory for second order equation. Derivation of such theory for second order equation is very similar to one for first order. Main ideas are the same.

General multistep method for second order equation $\ddot{y} = f(t, y)$ can be written in form

$$\sum_{j=0}^{k} \alpha_j y_{n+j} = \Delta t^2 \sum_{j=0}^{k} \beta_j f_{n+j}, \tag{4.2.14}$$

where Δt is the time step. We use notation $y_k = y(t_k)$, where $t_k = \Delta t k$. For method (4.2.14) first and second characteristic polynomials are defined by

$$\rho(\xi) = \sum_{j=0}^{k} \alpha_j \xi^j, \qquad \sigma(\xi) = \sum_{j=0}^{k} \beta_j \xi^j. \tag{4.2.15}$$

Local discretization error can be expressed by

$$\mathcal{L}[y(t), \Delta t] = \sum_{j=0}^{k} [\alpha_j y(t + j\Delta t) - \Delta t^2 \beta_j \ddot{y}(t + jh)], \tag{4.2.16}$$

assuming that y has as many derivatives as we need for this definition. Taylor expansion around point t gives

$$\mathcal{L}[y(t), \Delta t] = C_0 y(t) + C_1 \Delta t \dot{y}(t) + ... + C_q \Delta t^q y^{(q)}(t) + o(h^{q+1}). \tag{4.2.17}$$

Coefficients C_q have form:

$$C_0 = \sum_{j=0}^{k} \alpha_j, \tag{4.2.18a}$$

$$C_1 = \alpha_1 + 2\alpha_2 + ... + k\alpha_k, \tag{4.2.18b}$$

$$C_2 = \frac{1}{2!}(\alpha_1 + 2^2\alpha_2 + ... + k^2\alpha_k) - \sum_{j=0}^{k} \beta_j, \tag{4.2.18c}$$

$$C_q = \frac{1}{q!}(\alpha_1 + 2^q\alpha_2 + ... + k^q\alpha_q) - \tag{4.2.18d}$$

$$\frac{1}{(q-2)!}(\beta_1 + 2^{q-2}\beta_2 + ... + k^{q-2}\beta_k) \quad q = 3, 4, ... \quad .$$

Definition 4.2.1. *The multistep method is said to be of order p if $C_0 = C_1 = ... = C_{p+1} = 0$ and $C_{p+2} \neq 0$.*

Concerning stability, it can be shown that total error $\tilde{e}_n = y(t_n) - \tilde{y}_n$, where $\{\tilde{y}_n\}$ is the approximate solution, satisfies equation

$$\tilde{e}_n = \sum_{s=1}^{k} d_s r_s^n - \frac{\Phi}{\Delta t^2}\lambda \sum_{j=0}^{k} \beta_j, \tag{4.2.19}$$

where d_s are arbitrary constants, r_s are roots of stability polynomial[2]. Stability polynomial is defined by

$$\pi(r, h) = \rho(r) - h\sigma(r), \qquad h = \Delta t^2 \lambda. \tag{4.2.20}$$

Definition 4.2.2. *Method is called* absolutely stable*, if for a given h all roots of* (4.2.19) *satisfy $|r_s| \leq 1$ for $s = 1, 2, ..., k$.*

The importance of absolute stability rests in the fact that the total error $\tilde{e}_n$ remains bounded. We can now turn our attention to the particular case of scheme (4.2.12).

Order and stability

For the purpose of the discussion of method (4.2.12) we will not consider right hand side terms. In the view of subsection 4.2.1 we can reduce our

[2]During the derivation of this relation derivative $\frac{\partial f(t,y)}{\partial y} = \lambda$ was assumed constant, and local truncation error $\Phi_n = \Phi$ was also assumed constant. In our linear case the assumption on λ is satisfied exactly

attention on scalar equation $\ddot{y}+\omega^2 y=0$. If we apply the scheme introduced at the beginning of this subsection, we will arrive at $y^{i+2}-2y^{i+1}+y^i = \frac{\Delta t^2\omega^2}{2}(y^{i+2}+y^i)$. Following notation introduced for discussion of multistep methods, this particular method is characterized by parameters

$$k=2 \tag{4.2.21a}$$

$$\alpha_0=1 \qquad \beta_0=\frac{1}{2} \tag{4.2.21b}$$

$$\alpha_1=-2 \qquad \beta_1=0 \tag{4.2.21c}$$

$$\alpha_2=1 \qquad \beta_2=\frac{1}{2}, \tag{4.2.21d}$$

$$\tag{4.2.21e}$$

and first and second characteristic polynomials are

$$\rho(\xi)=(\xi-1)^2, \qquad \sigma(\xi)=\frac{1}{2}(\xi^2+1). \tag{4.2.22}$$

We immediately see, recalling definition 4.2.1, that the method is of order 2. Stability will be investigated through properties of stability polynomial (4.2.19). Again, it is sufficient to analyze equation $\ddot{y}=-\omega^2 y$, $\omega>0$. In this case $\lambda=-\omega^2$. Stability polynomial then takes form

$$\pi(r,h)=\left(1+\frac{1}{2}\Delta t^2\omega^2\right)r^2-2r+\left(1+\frac{1}{2}\Delta t^2\omega^2\right). \tag{4.2.23}$$

Roots of this polynomial are:

$$r_{1,2}=\frac{1\pm i\sqrt{2(\frac{1}{2}\Delta t^2\omega^2)+(\frac{1}{2}\Delta t^2\omega^2)^2}}{1+\frac{1}{2}\Delta t^2\omega^2}. \tag{4.2.24}$$

Computation of norm for both roots shows that $|r_{1,2}|=1$ regardless on timestep Δt. We can therefore say that the method is absolutely stable for equation $\ddot{y}=-\omega^2 y$ and then for our equation $D\ddot{\boldsymbol{c}}+A\boldsymbol{c}=0$. Since the absolute stability does not depend of the time step Δt, we can talk about unconditional stability.

4.2.3 Bossak-Newmark scheme

Consider a set of linear second order differential equations in form[3]

$$D\ddot{\boldsymbol{c}}+C\dot{\boldsymbol{c}}+A\boldsymbol{c}=F, \tag{4.2.25}$$

[3]Let me remark that in our case no damping matrix will be present, but the Bossak-Newmark scheme will be shown with it.

where D is the mass matrix, C is the damping matrix and A is the stiffness matrix. Bossak, Wood and Zienkiewicz proposed the following algorithm based on Newmark scheme for integrating this system of ODEs [17]:

$$\boldsymbol{c}^{i+1} = \boldsymbol{c}^i + \Delta t \dot{\boldsymbol{c}}^n + (\Delta t)^2 \left(\frac{1}{2} - \beta\right) \ddot{\boldsymbol{c}}^i + (\Delta t)^2 \beta \ddot{\boldsymbol{c}}^{i+1}, \tag{4.2.26}$$

$$\dot{\boldsymbol{c}}^{i+1} = \dot{\boldsymbol{c}}^n + \Delta t(1-\gamma)\ddot{\boldsymbol{c}}^i + \Delta t \gamma \ddot{\boldsymbol{c}}^{i+1}, \tag{4.2.27}$$

$$(1-\alpha)D\ddot{\boldsymbol{c}}^{i+1} + \alpha D\ddot{\boldsymbol{c}}^i + C\dot{\boldsymbol{c}}^{i+1} + A\boldsymbol{c}^{i+1} = F^{i+1}. \tag{4.2.28}$$

In the case of $\alpha = 0$ this algorithm reduces to Newmark's method [14]. Additional parameter α was added to the scheme to introduce artificial damping. The purpose of this numerical dissipation is to reduce spurious oscillations, which sometimes occur during the computation. For $\alpha = 0$ we get no additional dissipation. The method is referred to in literature as WBZ-α method, each letter for one author, namely Wood, Bossak, Zienkiewicz.

The aim of artificial damping introduced by the presence of parameter α is to damp high frequency oscillations. The method is commonly used on the system of equations coming from FEM spatial discretization. Spatial resolution of finite elements may be poor, so it is desirable to damp out high frequency modes. There were efforts to design a method which would not dissipate much at lower frequencies while maintaining its dissipation at high frequencies. Bossak's method is a member of such family of methods. The most recent one was proposed by Chung and Hulbert. The method is called *the generalized-α method* [5]. The generalized-α method ensures that for desired amount of high frequency dissipation the low frequency dissipation is minimized. We use slightly less complicated Bossak-Newmark method.

Performance of the scheme is controlled by three parameters α, β, γ. To get a second order accuracy with unconditional stability, we have to satisfy conditions

$$\beta \geq \frac{\gamma}{2} \geq \frac{1}{4}, \qquad \alpha = \frac{1}{2} - \gamma. \tag{4.2.29}$$

To obtain a second order method that is unconditionally stable with positive artificial damping, condition (4.2.29) must be satisfied with sharp inequalities

$$\beta > \frac{\gamma}{2} > \frac{1}{4}, \qquad \alpha = \frac{1}{2} - \gamma. \tag{4.2.30}$$

The above conditions are derived from theory of multi-step linear methods of second order. The theory is discussed for example in [9, pg. 253-260]. Authors derived conditions for stability and second order from analysis of the method for equation $\ddot{y} + \omega^2 y = 0$, $\omega > 0$. Authors show that for this equation the method is equivalent to a four step linear method.

Equation for $\boldsymbol{c}^{n+1}$

Equations (4.2.26), (4.2.27), (4.2.28) reveal the principle of the method but are useless when one wants to really use it. These equations have to be slightly modified in order to get an equation for displacement on the next time level. This is one of ways to get the equation for $\boldsymbol{c}^{n+1}$. From (4.2.26) express the acceleration on (n+1)th time level

$$\ddot{\boldsymbol{c}}^{i+1} = \frac{1}{\beta(\Delta t)^2}(\boldsymbol{c}^{i+1} - \boldsymbol{c}^i) - \frac{1}{\beta\Delta t}\dot{\boldsymbol{c}}^i + \left(1 - \frac{1}{2\beta}\right)\ddot{\boldsymbol{c}}^i. \tag{4.2.31}$$

Substitute from the above equation into (4.2.27) for $\boldsymbol{c}^{n+1}$ to obtain

$$\dot{\boldsymbol{c}}^{i+1} = \frac{\gamma}{\beta\Delta t}(\boldsymbol{c}^{i+1} - \boldsymbol{c}^i) + \left(1 - \frac{\gamma}{\beta}\right)\dot{\boldsymbol{c}}^i + \Delta t\left(1 - \frac{\gamma}{2\beta}\right)\ddot{\boldsymbol{c}}^i. \tag{4.2.32}$$

Finally substitute (4.2.31), (4.2.32) into equation (4.2.28) to get

$$\begin{aligned}\left[\frac{1-\alpha}{\beta(\Delta t)^2}D + C\frac{\gamma}{\beta\Delta t} + A\right]\boldsymbol{c}^{i+1} = F_{i+1} + \\ D\left[\frac{1-\alpha}{\beta(\Delta t)^2}\boldsymbol{c}^i + \frac{1-\alpha}{\beta\Delta t}\dot{\boldsymbol{c}}^i - \left(1 + \frac{\alpha-1}{2\beta}\right)\ddot{\boldsymbol{c}}^i\right] + \\ C\left[\frac{\gamma}{\beta\Delta t}\boldsymbol{c}^i + \left(\frac{\gamma}{\beta} - 1\right)\dot{\boldsymbol{c}}^i + \Delta t\left(\frac{\gamma}{2\beta} - 1\right)\ddot{\boldsymbol{c}}^i\right].\end{aligned} \tag{4.2.33}$$

A simpler version of the equation without damping matrix C which we actually use is written as

$$\left[\frac{1-\alpha}{\beta(\Delta t)^2}D + A\right]\boldsymbol{c}^{i+1} = F_{i+1} + D\left[\frac{1-\alpha}{\beta(\Delta t)^2}\boldsymbol{c}^i + \frac{1-\alpha}{\beta\Delta t}\dot{\boldsymbol{c}}^i - \left(1 + \frac{\alpha-1}{2\beta}\right)\ddot{\boldsymbol{c}}^i\right]. \tag{4.2.34}$$

When we have a solution $\boldsymbol{c}^{i+1}$ we can compute velocity and acceleration on $(i+1)$th time level. First compute the acceleration and finally compute velocity on the next time level:

$$\ddot{\boldsymbol{c}}^{i+1} = \frac{1}{\beta(\Delta t)^2}(\boldsymbol{c}^{i+1} - \boldsymbol{c}^i) - \frac{1}{\beta\Delta t}\dot{\boldsymbol{c}}^i + \left(1 - \frac{1}{2\beta}\right)\ddot{\boldsymbol{c}}^i, \tag{4.2.35}$$

$$\dot{\boldsymbol{c}}^{i+1} = \dot{\boldsymbol{c}}^i + \Delta t(1-\gamma)\ddot{\boldsymbol{c}}^i + \gamma\Delta t\ddot{\boldsymbol{c}}^{i+1}. \tag{4.2.36}$$

Bossak-Newmark's advantage is that we automatically obtain approximation for velocity and acceleration.

Let me add one remark concerning the actual implementation. In order to maximize performance of the method, it is reasonable to use all the information we have about the problem. Since we have to solve a system of linear

algebraic equations on each time level, it would be nice if we had a way to accelerate the computation. A small amount of effort can be saved by properly choosing the first approximation for the solution of equation (4.2.34). The closer to actual solution we choose the first approximation, the less iterations we have to compute. We can make use of our knowledge of displacement, velocity and acceleration on the i-th level by using Taylor expansion to get as close as possible to the next time level solution. We can express this idea by

$$\boldsymbol{c}_{CG0}^{i+1} = \boldsymbol{c}^i + \Delta t \dot{\boldsymbol{c}}^i + \frac{1}{2}(\Delta t)^2 \ddot{\boldsymbol{c}}^i. \tag{4.2.37}$$

Subscript $CG0$ denotes the starting approximation of solution for CG algorithm. This approach actually saves a few iterations.

4.3 Energy balance

Energy balance can be formally obtained after testing the weak formulation by velocity $\dot{\boldsymbol{u}}$. This discussion follows [16]. We do not bother with the question whether velocity is sufficiently smooth do so at the moment. Consider $\boldsymbol{u}$ which is a weak solution of the problem and satisfies

$$\int_\Omega \rho \ddot{\boldsymbol{u}} \cdot \boldsymbol{v} \,\mathrm{d}x + \int_\Omega \boldsymbol{\tau} : \boldsymbol{\varepsilon}(\boldsymbol{v}) \,\mathrm{d}x = \int_\Omega \boldsymbol{f} \cdot \boldsymbol{u} \,\mathrm{d}x \quad \boldsymbol{v} \in V. \tag{4.3.1}$$

Note, that the solution $\boldsymbol{u}$ possesses a discontinuity across Γ as demanded by boundary conditions (2.1.5a), (2.1.5b) and therefore such a function does not belong to the space of test functions V. Nevertheless, a function which does belong there is $\boldsymbol{u} - \boldsymbol{u}_\Gamma$, where $\boldsymbol{u}_\Gamma$ is an extension of discontinuity function $\boldsymbol{f}_\Gamma$ into region Ω_Γ. We assume that $\boldsymbol{u}_\Gamma$ satisfies conditions which where demanded on it in discussion about weak solution. Such a function no longer has a discontinuity across Γ and neither does its time derivative $[\boldsymbol{u} - \boldsymbol{u}_\Gamma]_-^+ = 0 = [\dot{\boldsymbol{u}} - \dot{\boldsymbol{u}}_\Gamma]_-^+$. Assume that $\dot{\boldsymbol{u}} - \dot{\boldsymbol{u}}_\Gamma$ can be used as a test function to get

$$\int_\Omega \rho \ddot{\boldsymbol{u}} \cdot \dot{\boldsymbol{u}} \,\mathrm{d}x + \int_\Omega \boldsymbol{\tau} : \boldsymbol{\varepsilon}(\dot{\boldsymbol{u}}) \,\mathrm{d}x = \int_\Omega \boldsymbol{f} \cdot \dot{\boldsymbol{u}} \,\mathrm{d}x + E_d(\dot{\boldsymbol{f}}_\Gamma), \tag{4.3.2}$$

where we have used the abbreviation

$$E_d(\boldsymbol{f}_\Gamma) := \int_{\Omega_\Gamma} \rho \ddot{\boldsymbol{u}} \cdot \boldsymbol{u}_\Gamma \,\mathrm{d}x + \int_{\Omega_\Gamma} \boldsymbol{\tau}(\boldsymbol{u}) : \boldsymbol{\varepsilon}(\boldsymbol{u}_\Gamma) \,\mathrm{d}x - \int_{\Omega_\Gamma} \boldsymbol{f} \cdot \boldsymbol{u}_\Gamma \,\mathrm{d}x, \tag{4.3.3}$$

where $\boldsymbol{u}_\Gamma$ is an extension of $\boldsymbol{f}_\Gamma$ into region Ω_Γ. Value E_d really depends only on the discontinuity prescribed and not on the extension $\boldsymbol{u}_\Gamma$ which was used.

Let there be two extensions $\boldsymbol{u}_\Gamma^1$ and $\boldsymbol{u}_\Gamma^2$ of the same discontinuity function $\boldsymbol{f}_\Gamma$ which thus satisfy $(\boldsymbol{u}_\Gamma^1 - \boldsymbol{u}_\Gamma^2)|_\Gamma = 0$. Then functional E_d gives

$$E_d(0) = \int_{\Omega_\Gamma} \rho\ddot{\boldsymbol{u}}\cdot(\boldsymbol{u}_\Gamma^1 - \boldsymbol{u}_\Gamma^2)\,\mathrm{d}x + \int_{\Omega_\Gamma} \boldsymbol{\tau}(\boldsymbol{u}) : \boldsymbol{\varepsilon}\big(\boldsymbol{u}_\Gamma^1 - \boldsymbol{u}_\Gamma^2\big)\,\mathrm{d}x - \int_{\Omega_\Gamma} \boldsymbol{f}\cdot(\boldsymbol{u}_\Gamma^1 - \boldsymbol{u}_\Gamma^2)\,\mathrm{d}x = 0. \tag{4.3.4}$$

This equality holds because $\boldsymbol{u}$ is a solution and therefore it satisfies (4.3.1). The difference of two extensions $\boldsymbol{z} := \boldsymbol{u}_\Gamma^1 - \boldsymbol{u}_\Gamma^2$ then belongs to $W_0^{1,2}(\Omega_\Gamma;\mathbb{R}^3)$. Such functions can be extended by zero to the whole region Ω. Therefore $\boldsymbol{z}$ (extended by zero) is an admissible test function from V and the identity holds. Functional $E_d(\dot{\boldsymbol{f}}_\Gamma)$ has a meaning of power generated by the discontinuity in displacement on Γ.

Consider a general case of Hook's law, where $\boldsymbol{\tau} = \mathbb{C}\boldsymbol{\varepsilon}(\boldsymbol{u})$. Using this notation, we can rewrite expression (4.3.2) into

$$\frac{d}{dt}\int_\Omega \frac{\rho}{2}\,|\dot{\boldsymbol{u}}|^2\,\mathrm{d}x + \frac{d}{dt}\int_\Omega \frac{1}{2}\boldsymbol{\varepsilon}(\boldsymbol{u}) : \mathbb{C}\boldsymbol{\varepsilon}(\boldsymbol{u})\,\mathrm{d}x = \int_\Omega \boldsymbol{f}\cdot\dot{\boldsymbol{u}}\,\mathrm{d}x + E_d(\dot{\boldsymbol{f}}_\Gamma), \tag{4.3.5}$$

where we can see clearly the meaning of each term. The first term on the left-hand side is a rate of change of kinetic energy. The second term on the left-hand side represents the rate of change of stored energy in the elastic medium. First term on the right-hand side represents the power of volume forces. The last term on the left-hand side has a meaning of power generated by the prescribed discontinuity in displacement.

4.3.1 Energy balance in the approximate solution

In this subsection $\boldsymbol{u}$ denotes an approximate solution, which is a linear combination of basis functions of V_h. Kinetic energy in the approximate solution can be expressed as

$$E_{kin} = \int_\Omega \frac{\rho}{2}\dot{\boldsymbol{u}}\cdot\dot{\boldsymbol{u}}\,\mathrm{d}x = \sum_{i,j}\frac{1}{2}\dot{\boldsymbol{c}}_i\dot{\boldsymbol{c}}_j\int_\Omega \rho\boldsymbol{v}_i\cdot\boldsymbol{v}_j\,\mathrm{d}x = \frac{1}{2}\dot{\boldsymbol{c}}\cdot D\dot{\boldsymbol{c}}, \tag{4.3.6}$$

where $\boldsymbol{c}$ is a vector of coefficients of $\boldsymbol{u}$ in the basis of $\{\boldsymbol{v}_i\}$.

Stored elastic energy in the approximate solution can be expressed similarly

$$E_{ela} = \int_\Omega \frac{1}{2}\boldsymbol{\tau} : \boldsymbol{\varepsilon}(\boldsymbol{u})\,\mathrm{d}x = \sum_{i,j}\frac{1}{2}\boldsymbol{c}_i\boldsymbol{c}_j\int_\Omega \lambda(\nabla\cdot\boldsymbol{v}_i)(\nabla\cdot\boldsymbol{v}_j) + 2\mu\boldsymbol{\varepsilon}(\boldsymbol{v}_i) : \boldsymbol{\varepsilon}(\boldsymbol{v}_j)\,\mathrm{d}x = \frac{1}{2}\boldsymbol{c}\cdot A\boldsymbol{c}. \tag{4.3.7}$$

Relations (4.3.6) and (4.3.7) provide an easy way to compute the kinetic and elastic energy in the approximate solution. Using these we can investigate

conservation of energy in the particular time-integration algorithm. Although this is not an exact proof, we also immediately see that matrices A, D must be positive definite. The reason is that they are operators that produce elastic and kinetic energy respectively. One always expects these two kinds of energy to be nonnegative. For the matrix A the positive definiteness follows from V ellipticity of bilinear operator A. Positive definiteness is important, because we finally end up solving systems of linear equations with these matrices on the left-hand side. Since matrices are also symmetric, we can use the method of conjugate gradients to solve the system. We will present plots of total energy versus time in later sections which show actual results of computations to show that time-integration schemes really conserve energy.

4.4 Implementation

The first step in carrying out computation is to generate a suitable mesh. In our case we have chosen to use tetrahedral elements with first order approximation. For generation of meshes we use Netgen 4.4 [2]. Netgen is suitable for generating tetrahedral meshes for domains with not too complicated geometry. The geometry of domain is defined by making unions, intersections, differences of simple geometric entities. These entities are for example a half-space, a cylinder, a sphere, a cone. Netgen also provides a simple way to define granularity of the mesh. Having a possibility to alter coarseness is crucial, because we would like to reach a compromise between discretization error and computational effort.

I have developed a simple program which takes the mesh generated by Netgen, computes matrix entries and solves the systems of linear equations defined by them. Since the matrix A is symmetric and positive definite, the method of conjugate gradients can be applied to solve the system (either in static or dynamic case).

The program uses library SparseLib++ [3]. It is an object oriented library designed to deal with sparse matrices. It offers advantages of object oriented design while maintaining speed of matrix vector multiplication. The multiplication is computed with help of routines from BLAS, so speed is guaranteed. Sparselib++ is accompanied by library IML++, which implements iterative methods for solving linear algebraic systems. Although it offers many methods for more general matrices, we use conjugate gradients because our matrix which defines the system is always symmetric and positive definite.

Preconditioners are used in order to gain a faster convergence of CG. Incomplete Choleski preconditioner gives the best results (fastest convergence), but also spends a lot of memory. Convergence of approximations is

significantly slower with diagonal preconditioning than with Choleski preconditioning. However for cases, where the computer is likely to run out of memory, it is better to use diagonal preconditioner because it requires less memory. As a stopping criterion we use condition $\frac{||r||}{||b||} < TOL$, where r is the residual of current approximation, b is a left-hand side and TOL is an a priori given tolerance.

4.4.1 Building matrices

Both A and D have the same sparse structure. The sparse structure is determined by mesh geometry and a substantial role plays node numbering. The number of nonzero elements in the matrix is invariant with respect to the nodes numbering, but better numbering can bring most nonzero entries close to the diagonal. I did not experiment with nodes renumbering. The i, j-th entry is nonzero if supports of basis functions corresponding to these nodes have a nontrivial intersection. In the case of first-order approximation this demand is satisfied whenever nodes i and j are connected with an edge, or equivalently when there exists an element (tetrahedron) containing both nodes. A fast way to build the matrix is to use concept of element based assembly [8, pg.76,77]. At the beginning the sparse structure must be determined and all entries set to zero.

Consider that we are in scalar case and that the element's nodes numbers are: p_1, p_2, p_3, p_4. Then this element contributes to matrix entries with indices p_1p_1, p_1p_2, p_1p_3 and so on. The contributions are computed using a quadrature rule on the particular element. So in this case each element contributes to 4^2 entries. In our case we solve vector problem, so all matrices have dimension $3*$(number of nodes). Generally each element contributes to 12^2 entries in the vector case. Using this way to assemble matrices, we only have to go through each element once. Time consumed to assemble a matrix depends linearly on the number of elements.

Quadrature rules

When assembling matrix A, we integrate constants over each element, because gradients of basis functions are constant. Integral over the element is simply the constant multiplied by the volume of the element.

When computing entries of matrix D, we integrate a quadratic function. Therefore it is desirable to use a quadrature rule of a second order of accuracy. Let $\hat{K}$ be a reference element, see figure 4.1. All elements can be mapped on the reference element with an affine linear mapping of form $F(\boldsymbol{x}) = B\boldsymbol{x} + b$. Matrix B is nonsingular. Hence all computations of integrals can be done on

the reference element. Note that since the mapping F is linear, Jacobian is constant. I used the following *open* rule to get exact quadratures of quadratic function on the reference element

$$\int_{\hat{K}} f(\boldsymbol{x})\,\mathrm{d}x = \sum_{i=1}^{4} \omega_i f(\mathbf{n}_i) + E(f), \tag{4.4.1}$$

where $E(f)$ is an error of the rule, ω_i are weights and n_i are nodes of the rule. This particular rule is exact for polynomial functions of order less or equal to two. Weights of the rule are

$$\omega_i = \frac{1}{24} \quad \text{for} \quad i = 1..4. \tag{4.4.2}$$

If we denote by $a = \frac{5+3\sqrt{5}}{20}$ and $b = \frac{5-\sqrt{5}}{20}$, nodes can be expressed as

$$\mathbf{n}_1 = (a, b, b), \tag{4.4.3a}$$
$$\mathbf{n}_2 = (b, a, b), \tag{4.4.3b}$$
$$\mathbf{n}_3 = (b, b, a), \tag{4.4.3c}$$
$$\mathbf{n}_4 = (b, b, b). \tag{4.4.3d}$$

This particular quadrature rule can be found in [7].

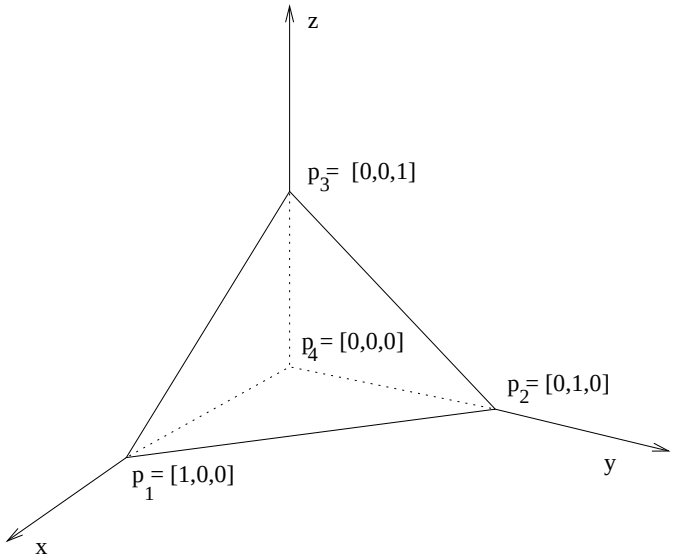

Figure 4.1: The reference element $\hat{K}$. All elements can me mapped on the reference element with an affine linear mapping of form $F(\boldsymbol{x}) = B\boldsymbol{x} + b$.

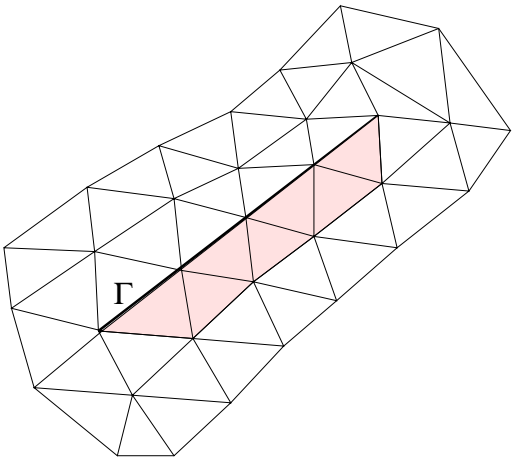

Figure 4.2: Situation in two dimensions. Support of discrete function $\boldsymbol{u}_\Gamma$ is colored in pink. In process of assembling matrices A_Γ and D_Γ we integrate only over elements which are pink.

4.4.2 Representation of the source function $\boldsymbol{u}_\Gamma$ in discrete form

The trick with assumption, that the solution is given as a sum of two components, is usually used when one needs to satisfy non-zero Dirichlet boundary conditions. Our setting of the problem shares the need of two-component solution with the case of non-zero Dirichlet boundary conditions. In order to simplify the following discussion and to avoid complicated notation, we will outline the idea for a scalar problem. The space V_h is generated by basis functions $\{\boldsymbol{v}_i\}_{i=1}^{DOF}$. Functions $\boldsymbol{v}_i$ are piecewise linear on each element and $\boldsymbol{v}_i(\boldsymbol{x}_j) = \delta_{ij}$ holds. If we want to capture the discontinuity, we must be able to generate a mesh, where element faces coincide with the fault surface.

Function $\boldsymbol{u}_\Gamma$ in discrete form: if $\boldsymbol{x}$ are coordinates of a node lying directly on Γ, then discrete version and the original $\boldsymbol{u}_\Gamma$ gives the same values. If the node is not on the fault surface Γ, then the discrete $\boldsymbol{u}_\Gamma$ is zero. Crucial moment is, that the discrete $\boldsymbol{u}_\Gamma$ is a linear combination of *modified basis functions*. The modification rests in a reduction of support of those basis functions, whose support spreads on both sides of the fault surface. If this is the case, then the new basis function remains untouched on the side of Γ where we add the source function. On the opposite side the function equals to zero. A modified basis function corresponding to $\boldsymbol{v}_i$ will be denoted by $\underline{\boldsymbol{v}}_i$. Note that such modified basis functions do not belong to V_h any more, because they are discontinuous.

Let's define matrices

$$(A_\Gamma)_{i,j} := A_h(\boldsymbol{v}_j, \underline{\boldsymbol{v}}_i), \tag{4.4.4}$$

$$(D_\Gamma)_{i,j} := (\boldsymbol{v}_i, \underline{\boldsymbol{v}}_j)_h. \tag{4.4.5}$$

The right-hand side contribution to the equation (4.1.5) coming from extension of slip function $\boldsymbol{u}_\Gamma = \sum_i (c_\Gamma)_i \underline{\boldsymbol{v}}_i$ can be very easily expressed in terms of the above matrices A_Γ and D_Γ:

$$D\ddot{\boldsymbol{c}} + A\boldsymbol{c} = F - A_\Gamma \boldsymbol{c}_\Gamma - D_\Gamma \ddot{\boldsymbol{c}}_\Gamma, \tag{4.4.6}$$

where $\boldsymbol{c}_\Gamma$ are coefficients of decomposition of discrete function $\boldsymbol{u}_\Gamma$ into modified basis functions and F denotes contribution of volume forces. Entries of matrices A_Γ, D_Γ can be computed the same way as the entries of A and D. The only change is, that we only consider contributions from elements, which lie on one particular side of the fault surface - see figure 4.2. Omitting elements from the opposite side ensures, that we cut off the support of basis functions which have its base node directly on Γ.

Chapter 5

Results

This chapter presents results achieved with the methods introduced in previous chapters and sections. The first part shows how finite elements work in the static case for two slip functions. The approximate solution is compared to an analytic solution for the first case of circular shear crack. Turning to time dependent slip function, there is no analytic solution available. Our data are compared to a reference solution obtained by the discrete wavenumber method. We use P^1 approximation for displacement field and stress field is then computed from displacement using Hook's law. Approximate solution for stresses is therefore a piecewise constant function.

All results show behavior of solution only relatively close to fault zone. If we wanted to accommodate a large neighbourhood of the fault into our computational domain, we would not be able to carry out the computation because of the size of the problem. Size of neighbourhood of the fault is limited by our hardware equipment.

Following two sections 5.1 and 5.2 show static modifications of problems defined at the beginning of this paper. Static equations are original equations defining the problem where term with $\ddot{\boldsymbol{u}}$ is omitted. In words of numerics we solve one system of equations for coefficients $\boldsymbol{c}$ of displacement field in the basis of V_h.

All quantities in equations are considered to be dimensionless.

5.1 The static circular-crack model

Setting of this problem is well known, because an analytic solution exists for this problem. The problem is qualitatively discussed in [11]. Since there is an analytic solution, it was the first test of the method. The analytic solution, which is known for the case of whole $\mathbb{R}^3$, can be found in [4]. Of course, our

numerical results are computed on a bounded domain. Computed solution was compared to analytic solution directly on the fault plane and close to it. Since we are interested only in solution directly on the fault plane and close to it, the computational domain can be chosen relatively small. All meshes we used for computation had a shape of a sphere with radius equal to three. The sphere's centre is at the origin. Zero Dirichlet boundary conditions are prescribed on the whole boundary of Ω. Crack is represented as a circular fault zone of unit radius with the centre at the origin.

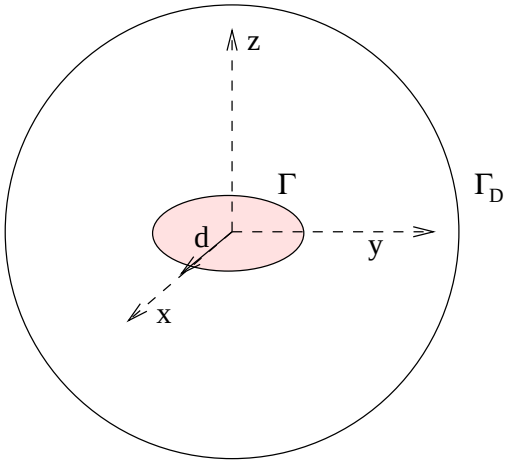

Figure 5.1: Schematically depicted computational domain for both circular-crack model and cosine slip model. Relative size of fault zone and bounding sphere is preserved. Vector $\boldsymbol{d}$ indicates direction of the slip.

The source is defined by

$$\Gamma = \{\boldsymbol{x} \in \mathbb{R}^3 : \boldsymbol{x}_3 = 0, \|\boldsymbol{x}\| < 1\}, \tag{5.1.1}$$

$$[\boldsymbol{u}]^+_- = \boldsymbol{e}_1 \frac{24}{7\pi}\sqrt{r^2-1}, \quad r \leq 1, \tag{5.1.2}$$

where $\boldsymbol{e}_i$ denotes unit vector in i-th direction and r denotes distance from the origin. Discontinuity on the fault plane Γ has a constant direction with a ball shaped amplitude.

The analytic solution for $\boldsymbol{\tau}$ is known in the fault plane $z = 0$:

$$\boldsymbol{\tau}_{13} = \begin{cases} -1 & \text{for } r < 1, \\ \frac{2}{\pi}\left[-\arctan(\sqrt{r^2-1}) + \frac{1}{\sqrt{r^2-1}} + \frac{1}{7r^2}\frac{1}{\sqrt{r^2-1}}\cos(2\theta)\right] & \text{for } r > 1, \end{cases} \tag{5.1.3}$$

where θ is an angle between radius vector $\boldsymbol{r}$ and $\boldsymbol{e}_1$. Distance from the origin is denoted by $r = |\boldsymbol{r}|$. Note that the analytic solution for stress has

a singularity at $r = 1$. Analytic solution is known for all stress components, but we present only one. Results of the benchmark for the static problem defined by (5.1.1), (5.1.2) are shown in figure 5.2.

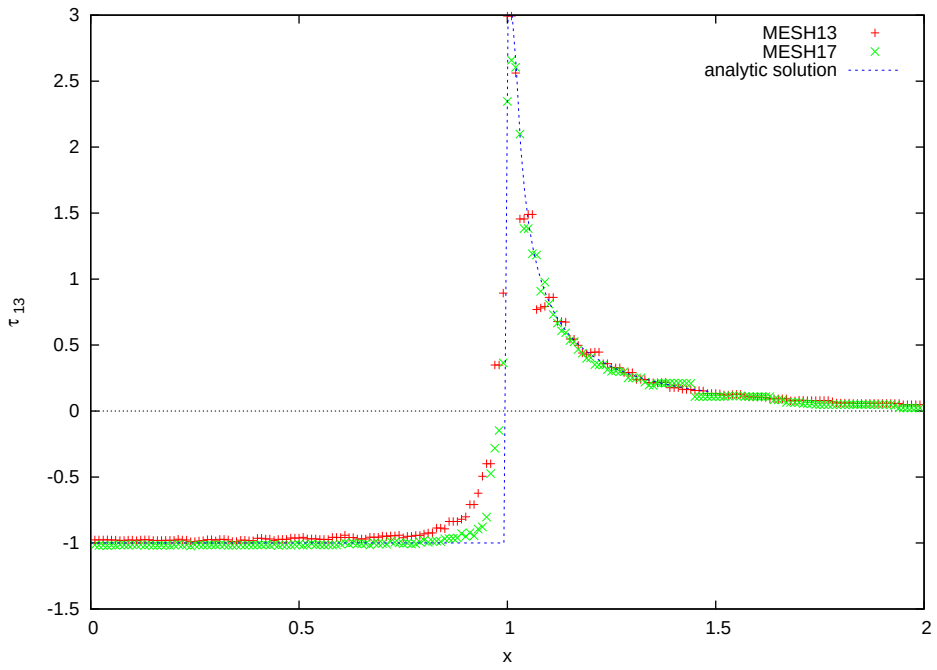

Figure 5.2: Plot shows $\boldsymbol{\tau}_{13}(x, 0, 0)$ on the first coordinate axis. Crosses refer to two meshes on which the computation was carried out. In MESH13, element diameter directly on the fault plane Γ was $diam(K) \sim 0.03$. MESH17 had the element diameter $diam(K) \sim 0.015$.

We can see, that refining the mesh results in a better approximation of the analytic solution. As the caption attached to the figure suggests, the second approximate solution is computed on elements half the size of those in the first solution (this holds only for elements directly on Γ). We can also see, that although computational domain is relatively small, it gives quite good approximation for the stress outside the crack.

Presence of the singularity in analytic solution suggested that we should try to compare our approximate solution also in a case where stresses are smooth. We believe that the singularity at unit circle is created by the fact, that the slip function is only C^0 on the unit circle. Therefore, the idea arises that if we prescribe slip function smooth on the boundary of Γ, it will give no singularity in stresses.

5.2 Cosine static slip

In the case of cosine static slip the fault plane Γ remains the same as in section 5.1. The only difference is in the prescribed slip function

$$[\boldsymbol{u}]_-^+ = \frac{1}{2}(\cos(\pi r) + 1)\boldsymbol{e}_1 \quad r \leq 1. \tag{5.2.1}$$

Slip amplitude has a shape of a cosine, while the slip direction remains parallel to x-axis. Unfortunately, now there is no analytic solution available. In order to verify our method we compare our results to a solution (which we call a reference solution) obtained by the discrete wavenumber method. Reference results, which contain data for stresses in the fault plane, were kindly provided by Jan Burjánek. The nature of discrete wavenumber method assumes that the problem is defined on whole $\mathbb{R}^3$. Results for cosine slip function are shown in figure 5.3. Note, that in the case of static cosine slip (5.2.1) we have used the same meshes as in the case of static circular-crack (5.1.2).

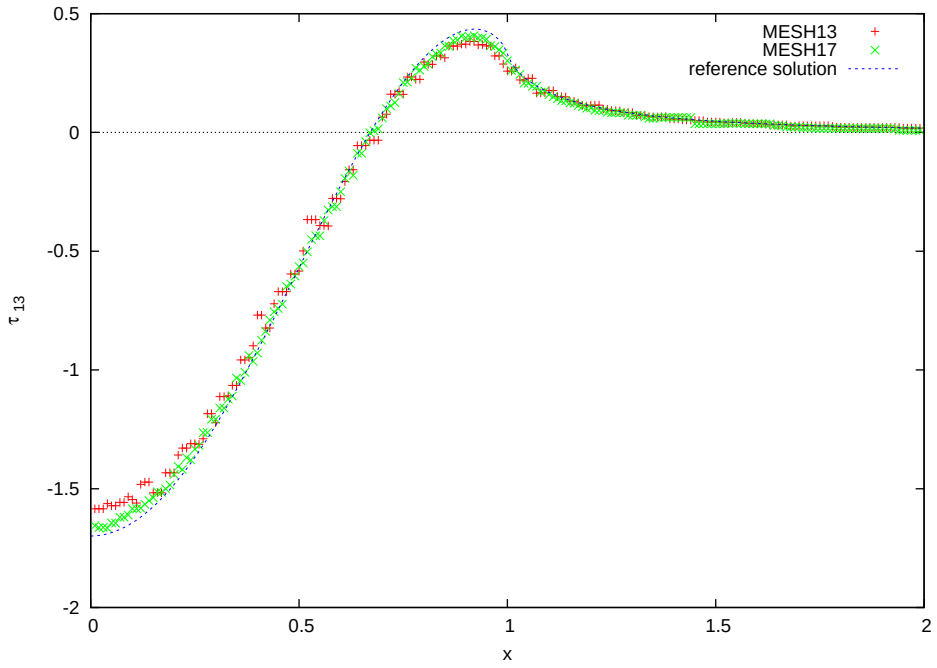

Figure 5.3: Plot presents the $\boldsymbol{\tau}_{13}(x, 0, 0)$ component as a function of x on the first coordinate axis. Reference solution is obtained by the discrete wavenumber method. Two colours of crosses refer to two meshes on which the computation was carried out. Element diameter on the fault plane for MESH13 was $diam(K) \sim 0.03$. For MESH17 the element diameter on the fault plane is $diam(K) \sim 0.015$.

Mesh is most refined on the fault plane, where we also present the results. If smaller elements are used, we get better agreement with the reference solution. This should not be surprising; finite elements just converge. One remark about presented figures 5.3, 5.2: stresses are symetric with respect to x, i.e. $\boldsymbol{\tau}_{13}(x,0,0) \approx \boldsymbol{\tau}_{13}(-x,0,0)$ for approximate solution. Therefore figures present solutions only for x positive.

5.3 Time dependent cosine slip

After we had gained some experience with static behaviour, we approached to the case with a time-dependent slip. Slip function, which was prescribed, will be shown in a few moments. At the initial time displacement and velocity fields are assumed to be zero. Orientation and position of the fault plane in space are the same as in the static case - see equation (5.1.1). The slip function which we prescribed was suggested by Jan Burjánek. The slip function describes propagation of rupture front with a constant rupture velocity. As soon as the rupture reaches a certain point, its slip varies in time from zero value to some static value. After reaching a static value of slip, it remains constant in time. Particular example of such a function is described by the following equations (5.3.2), (5.3.3), (5.3.4).

Static cosine slip function remains the same as in the static cosine slip

$$\boldsymbol{f}_r(r) = \frac{1}{2}\left[1 + \cos(\pi r)\right]\boldsymbol{e}_1, \qquad r \leq 1. \tag{5.3.1}$$

Rupture propagation begins at time t_0 at an initial point $\boldsymbol{x}_n = [0,0,0]$. Rupture front propagates with velocity v_r. As soon as the rupture reaches a certain point, displacement discontinuity at this point rises to a static value given by function $\boldsymbol{f}_r$. The rise has a duration t_n. There is no slip before rupture reaches this point.

$$[\boldsymbol{u}(r,t)]^+_- = 0 \quad \text{for} \quad t - t_0 < \frac{r}{v_r} \tag{5.3.2}$$

As soon as the rupture arrives, slip rises according to function given by the following equation

$$[\boldsymbol{u}(r,t)]^+_- = \frac{1}{2}\left[1 - \cos\left(\frac{\pi}{t_n}(t - \frac{r}{v_r} - t_0)\right)\right]\boldsymbol{f}_r(r) \tag{5.3.3}$$
$$\text{for} \quad \frac{r}{v_r} \leq t - t_0 \leq \frac{r}{v_r} + t_n.$$

As soon as the slip finishes rising, it remains constant and equal to the case of static cosine slip

$$[\boldsymbol{u}(r,t)]^+_- = \boldsymbol{u}_r(r) \quad \text{for} \quad \frac{r}{v_r} + t_n < t - t_0. \tag{5.3.4}$$

To be prepared completely for computation, we need to know second time derivative of the slip function, which is given by

$$[\ddot{\boldsymbol{u}}(r,t)]^+_- = \frac{\pi^2}{2{t_n}^2}\left[\cos\left(\frac{\pi}{t_n}(t - \frac{r}{v_r} - t_0)\right)\right]\boldsymbol{f}_r(r) \tag{5.3.5}$$
$$\text{for} \quad \frac{r}{v_r} + t_0 \le t - t_0 \le \frac{r}{v_r} + t_n$$

and equal to zero else.

The above definition of slip function can be rewritten in a more compact way using the Heaviside step function. To shorten the following formula, we use notation $t_r := t - t_0 - \frac{r}{v_r}$.

$$[\boldsymbol{u}(r,t)]^+_- = \frac{1}{2}\left\{\mathrm{H}(t_r)\left[1 - \cos\left(\frac{t_r}{t_n}\pi\right)\right] + \mathrm{H}(t_r - t_n)\left[1 + \cos\left(\frac{t_r}{t_n}\pi\right)\right]\right\}\boldsymbol{f}_r(r) \tag{5.3.6}$$

In our computations we have employed the following dimensionless values of parameters: $v_r = 0.8$, $t_n = 1$, $t_0 = 0$. The remaining parameters are $\lambda = 1.0$, $\mu = 1.0$, $\rho = 1.0$. With these parameters we get $c_p = \sqrt{\frac{\lambda+2\mu}{\rho}} = \sqrt{3}$. The relation between wave propagation speed and material parameters is derived for example in [12].

Figure 5.4 presents time dependence of energy (in the sense of section 4.3). Since initial conditions are zero for both displacement and velocity fields, initial energy is zero, too. As development of the rupture proceeds, energy rises to a nearly constant value, which is reached as soon as the slip function stops evolving. Presented graph shows how Bossak-Newmark scheme preserves energy. Energy in this particular situation remains constant to a relative error $\sim 10^{-4}$. All time-evolution problems were computed using Bossak-Newmark scheme. Central differences integration scheme gives the same results differing only in order of a truncation error.

Figures 5.5, 5.6 show behavior of our finite element solution. Results of our finite element computation were compared to a solution obtained using the discrete wavenumber method. We show graphs of $(1,3)$-th component of stress versus time at two points. Both points are in the fault plane. Point A is defined by coordinates $A = [2,0,0]$, while $B = [0,2,0]$. Time step used for

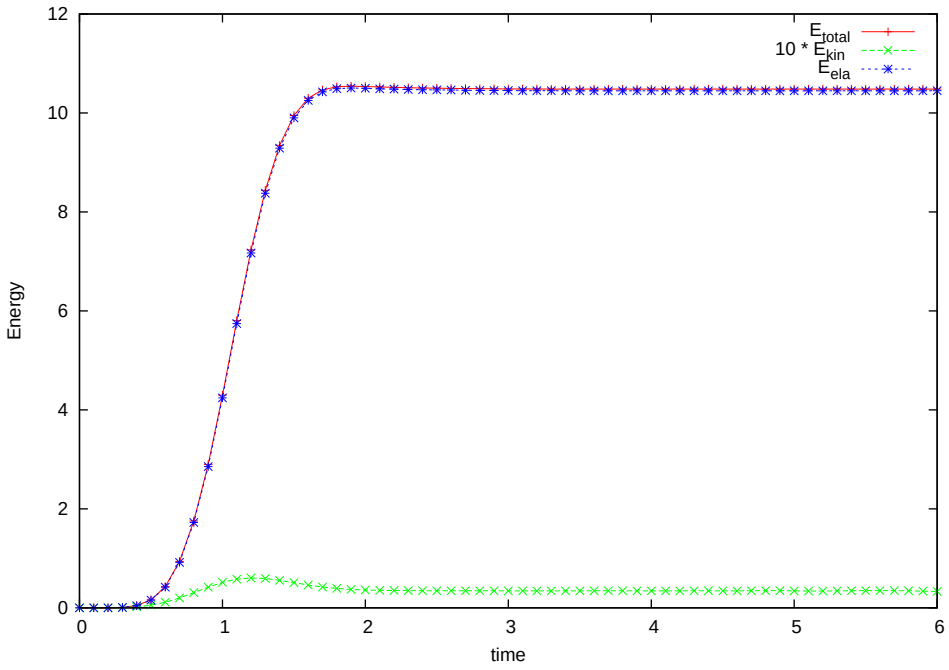

Figure 5.4: Time evolution of energy stored in solution. Kinetic energy is multiplied by factor 10.

this computation was $\Delta t = 0.02$. We can see that computed solution agrees quite well with solution produced by the discrete wavenumber method. Finite elements in addition produce artificial oscillations that have no physical background. We can see them in both graphs. One can reduce these oscillations by refining mesh. Ideal situation would be if we computed on a homogenous mesh with sufficiently small elements. This cannot be achieved in practice, because computational effort rises rapidly with refinement of the mesh. Presented figures were obtained from a solution computed on a mesh with about 200000 nodes and about 10^6 elements. It seems that spurious oscillations are present due to parts of the mesh that are coarsely discretized. If there are only small elements between source and receiver, we observe a significant reduction of these oscillations.

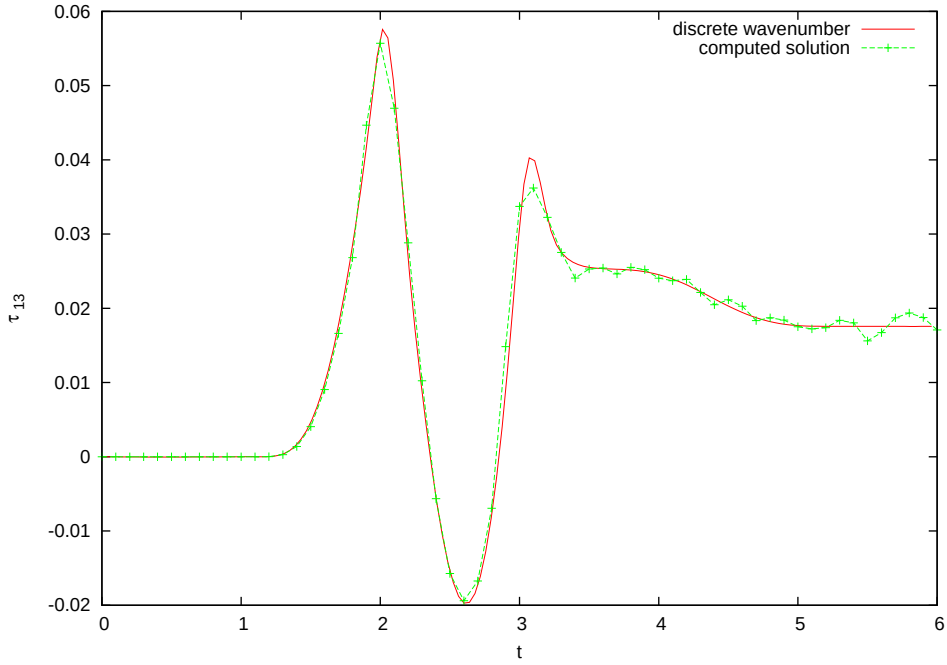

Figure 5.5: Time evolution of $\boldsymbol{\tau}_{13}$ at point $A = [2, 0, 0]$ compared to solution obtained with the discrete wavenumber method.

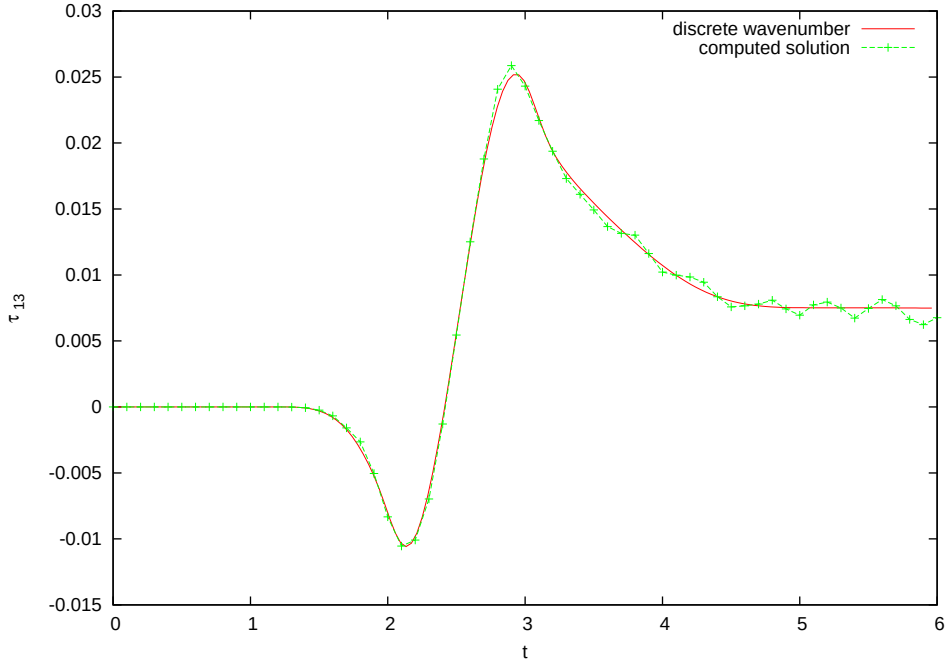

Figure 5.6: Time evolution of $\boldsymbol{\tau}_{13}$ at point $B = [0, 2, 0]$. Red line represents solution from the discrete wavenumber method.

5.4 Effects of mesh coarsening on spectra

To gain an insight into the reason why artificial oscillations appear, we studied spectra of seismograms for the previous problem setting. We focused our attention on effects caused by mesh coarsening.

Let T_S be the sampling period and its reciprocal value be the sampling frequency $f_S = 1/T_S$. Suppose we have a discrete signal $x[nT_S]$ where $n = 0..N-1$. Square brackets are used to emphasise that the signal is discrete. Signal discretization contains N samples. We consider the case with a purely real input signal.

Discrete Fourier transform is defined by

$$X[\omega_k] = \frac{1}{N} \sum_{n=0}^{N-1} x[nT_S] \exp(-\mathrm{i}\omega_k n), \tag{5.4.1}$$

where $\omega_k = \frac{2\pi k}{NT_S}$. We will limit our discussion of discrete Fourier transform only to its properties which are directly connected with our purpose - i.e. to study a spectrum of a discrete signal. Result of a discrete Fourier transform is a set of N complex numbers, which correctly scaled gives an information about the spectrum of the signal. Original signal $x[nT_S]$ can be expressed as a sum of complex exponentials

$$x[nT_S] = \sum_{k=0}^{N-1} X[\omega_k] \exp(\mathrm{i}nT_S\omega_k), \tag{5.4.2}$$

using its Fourier transform $X[\omega_k]$. Norms of complex numbers $X[\omega_k]$ give the amplitude with which the particular frequency $f_k = \frac{\omega_k}{2\pi}$ is contained in the signal $x[nT_s]$. If we wanted to directly evaluate quantities $X[\omega_k]$, it's time consumption would be of order N^2. The advantage of DFT is that there are algorithms which compute faster. Family of such algorithms is usually called Fast Fourier Transform. We use library FFTW 3.1.2 [1] in our computations, which is a well tested implementation of FFT written in C.

We have studied spectrum of artificial oscillations by the following procedure. We compared seismograms and their spectra for several receivers close to the source fault. Computation was done repeatedly on different meshes varying in elements diameter, because we wanted to study the effect of spatial resolution on artificial oscillations. Results were studied for three cases computed on different meshes. Each mesh was generated to have a different mean element diameter. With our hardware it is impossible to compute on completely homogenous mesh with reasonably small elements. Test meshes had a finely discretized inner ball of radius equal to 4 and a more coarsely

discretized outer ball with radius equal to 8. Boundary of the outer ball coincides with the boundary of domain Ω. Zero Dirichlet boundary conditions are prescribed on $\partial\Omega$. All receivers are contained in the inner ball. Three test meshes differ in diameter of elements in the inner ball. Outer ball discretization coarseness is the same for all meshes. The same holds for elements directly on the fault. Seismic source considered here is exactly the same as in the previous section 5.3.

Results of our investigation are presented in figures 5.7 and 5.8. Note that input signal is multiplied by an extended cosine bell window function which erases the ends of investigated interval. Extended cosine bell window function is defined by

$$b[n] = 1 \quad \text{for} \quad \frac{N}{10} \leq n \leq \frac{9N}{10} \quad \text{and} \quad b[n] = \frac{1}{2}\left[1 - cos\left(10\pi\frac{n}{N}\right)\right] \quad \text{else,} \tag{5.4.3}$$

where N is number of samples. Figures show seismograms for two receivers, plots for other receivers look qualitatively the same. Labelling of three lines follows the mean element diameter in the particular mesh. Although there are significant differences in plots of velocity versus time for three meshes, these do not seem to project into plots spectra with some simple pattern. In both sets of figures we can see repeating peak in frequency domain in the vicinity of 2 for mesh marked as diam 0.15, which vanishes as mesh is refined.

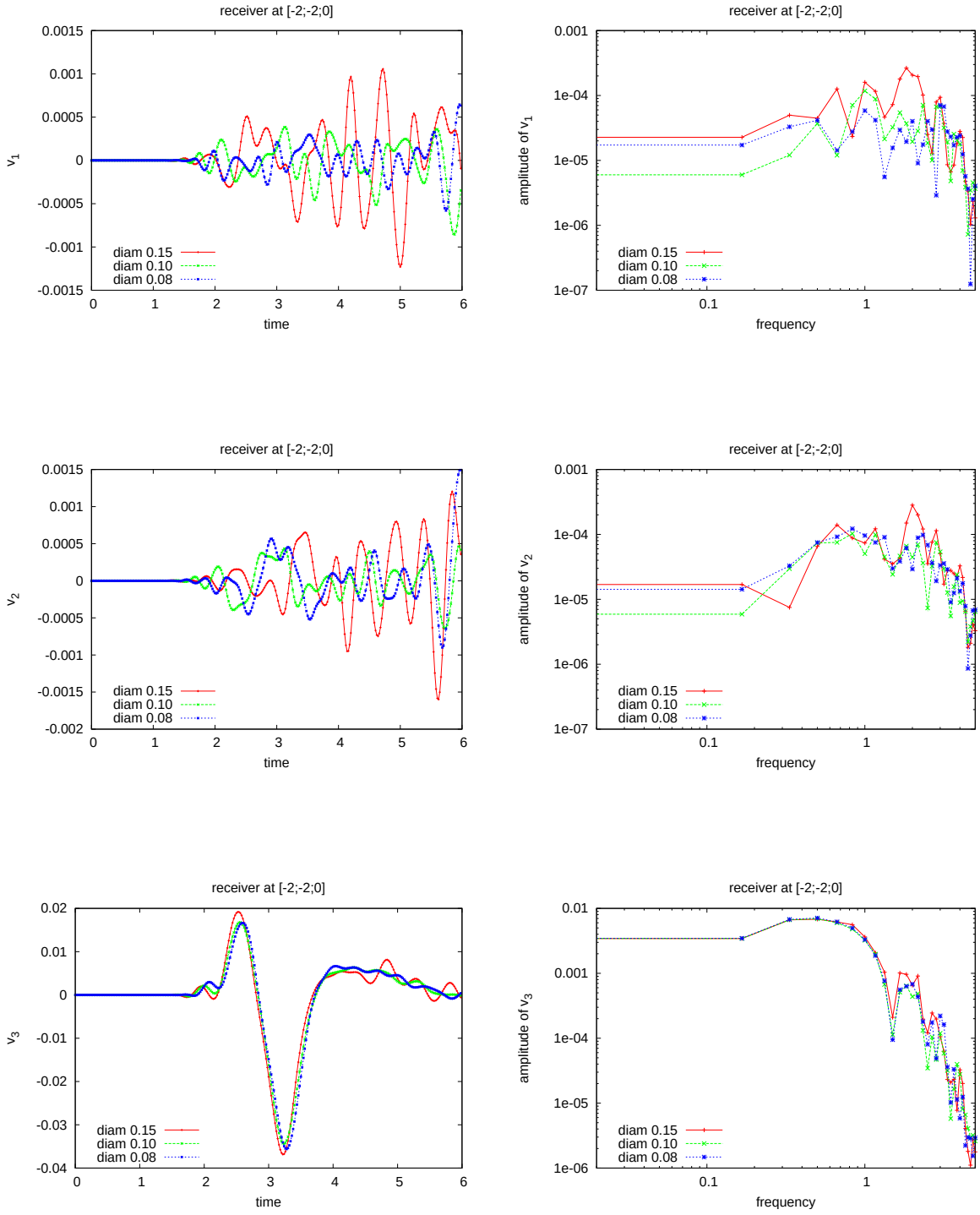

Figure 5.7: Seismograms and corresponding spectra of three velocity components for receiver at point [-2,-2,0].

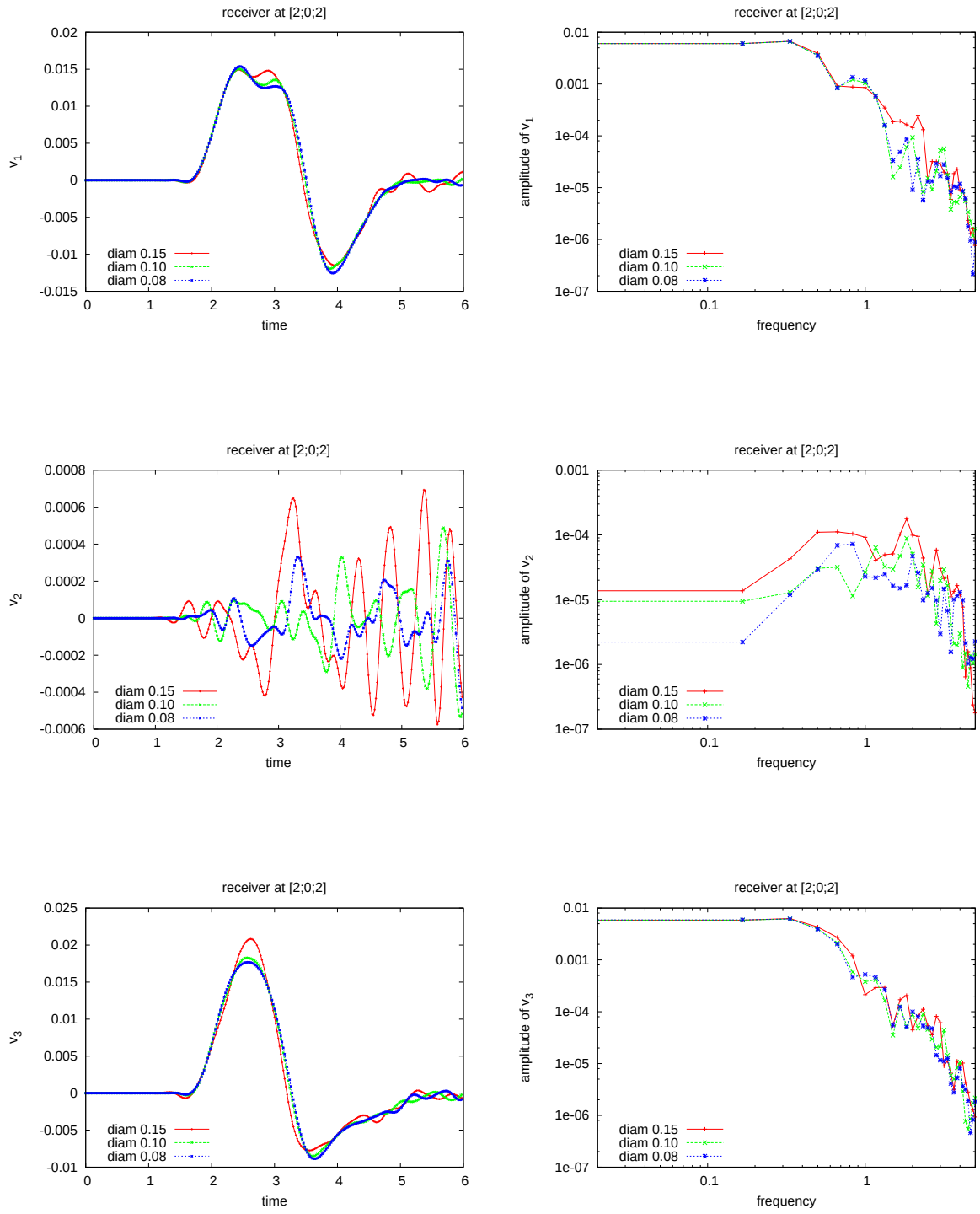

Figure 5.8: Seismograms and corresponding spectra of three velocity components for receiver at [2,0,2].

5.5 Piecewise planar fault surface

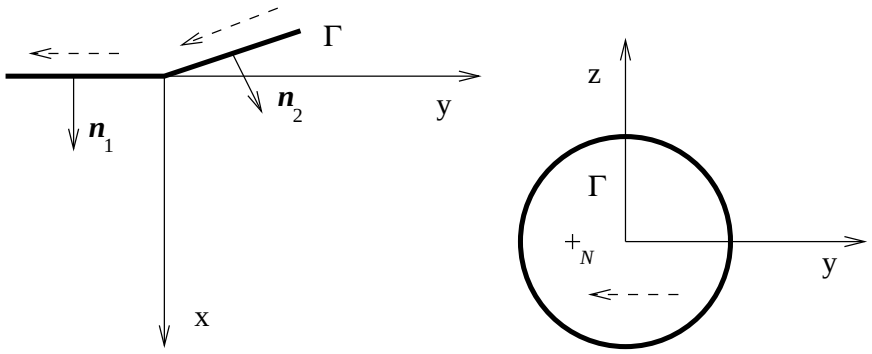

Figure 5.9: Geometry of a piecewise planar fault surface Γ. Dashed lines with arrows indicate slip direction. Point $N = [0.0, -0.5, 0.0]$ is a starting point for rupture propagation in the second case of our computation.

One of great advantages of finite elements is its ability to deal with complicated geometries. In majority of physical models of seismic source the fault zone is considered to be planar. In this section we weaken this assumption on the fault geometry and study effects which are caused by a more complicated fault geometry. We begin with a piecewise-planar fault, because it is the easiest natural way of complicating the fault geometry. In the following model we will assume that the fault surface Γ consists of two planar parts with slightly different normal vectors. Suggested geometry is schematically depicted in figure 5.9. Whole setting of the problem adopts many properties of the previous model with time-dependent cosine slip - recall section 5.3.

Similarly to the previous model the fault zone is a circle, but now it is oriented vertically. The slip function is the same as in the previous section. This also means that the amplitude of slip depends on the distance from the origin. Breaking the fault zone into two planar parts introduces a non-physical discontinuity in slip at the vertical line, which is an intersection of the two planes. This discontinuity would not appear if we considered slip which vanishes near the edge of fault zone. In numerical approximation there is an abrupt change in direction rather that a discontinuity. Direction of the slip is $-\boldsymbol{e}_2$ for the part of Γ whose normal is $\boldsymbol{n}_1$. On the second part of the fault whose normal is $\boldsymbol{n}_2$ slip direction is still in plane $z = 0$ and perpendicular to $\boldsymbol{n}_2$.

We have studied two cases which differ in the point from which fracture begins its propagation. In the first case, rupture propagates from the origin. Note that such a starting point lies directly on the intersection of two planes defining the fault zone. In the second case the initial point lies at the point

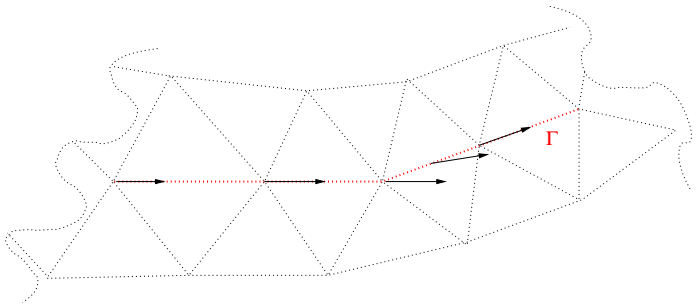

Figure 5.10: Slip direction on piecewise planar fault.

$N = [0.0, -0.5, 0.0]$. We can therefore look into effects which are caused by arrival of fracture to the edge in the fault geometry. We are also interested in resulting stresses in the vicinity of the fault zone.

In order to study dependence of resulting displacements and stresses on the fault geometry, we have carried out the computation for three configurations of geometry. Each fault zone consists of two planar parts, each part has a different normal vector. Two parts of piecewise planar fault zone intersect on the z-axis. One half of the fault zone remains untouched, while on the other half we add nonzero y component into the normal vector $\boldsymbol{n}_2$. We study three cases of fault geometries: cases are denoted by the y component of normal vector $\boldsymbol{n}_2$, while x component remains equal to unity and z component is zero. Normal vectors of two planar parts are:

$$\boldsymbol{n}_1^0 = (1.0, 0, 0) \quad \boldsymbol{n}_2^0 = (1, 0.0, 0), \tag{5.5.1}$$
$$\boldsymbol{n}_1^1 = (1.0, 0, 0) \quad \boldsymbol{n}_2^1 = (1, 0.1, 0), \tag{5.5.2}$$
$$\boldsymbol{n}_1^2 = (1.0, 0, 0) \quad \boldsymbol{n}_2^2 = (1, 0.2, 0). \tag{5.5.3}$$

Slip direction changes abruptly in the vicinity of intersection of two planes. In finite elements method we represent the source function $\boldsymbol{u}_\Gamma$ by its discrete version. Figure 5.10 shows slip direction behavior close to planes intersection. Direction changes linearly between two nodes. Note, that between two nodes where slip direction is different boundary condition (2.1.5a) that demanded slip to be tangent to Γ is violated. The region where such violation occurs only occupies width of the edge-neighboring element, as can be seen in figure 5.10.

Figures 5.11, 5.12, 5.13 present results for stress field in the plane $x = 0$. Each figure is titled by $\boldsymbol{n}_2^i$, where i refers to previously defined normal vectors of piecewise planar fault - recall (5.5.1)–(5.5.3). Because figures are generated at surface $x = 0$, for piecewise planar cases the second part of fault zone with normal vector $\boldsymbol{n}_2^i$ does not coincide with the plotting plane. That is the

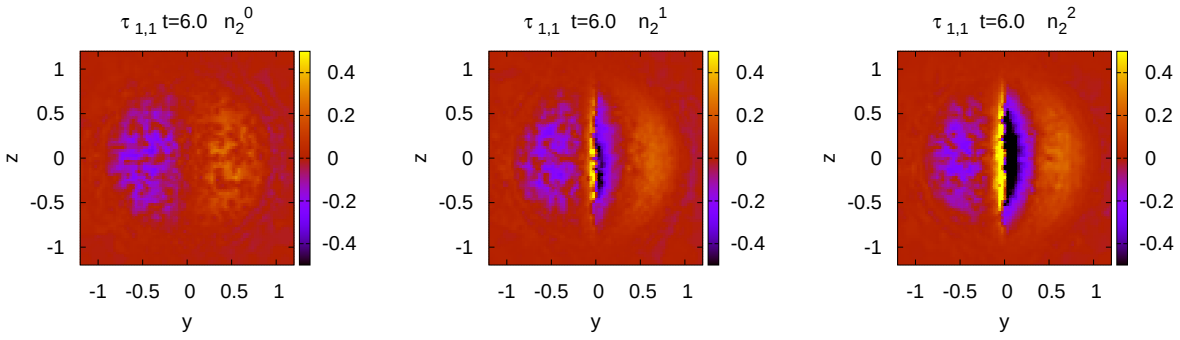

Figure 5.11: Fault normal force acting on the plane $x = 0$ at time $t = 6.0$.

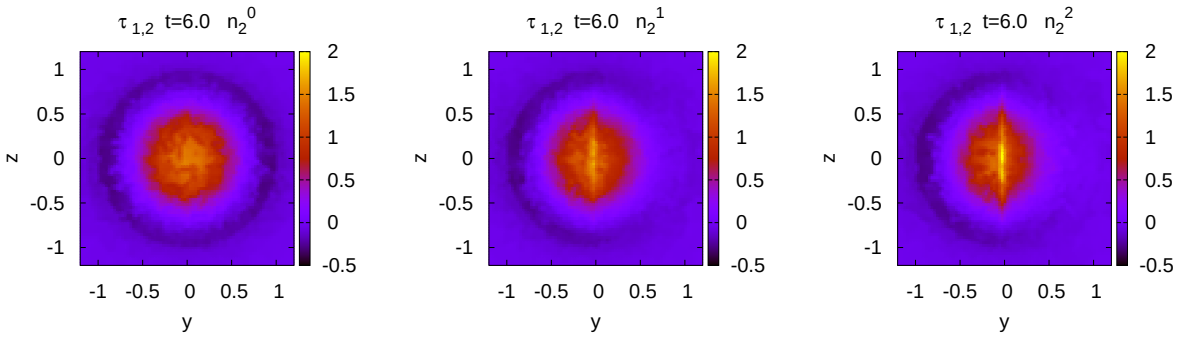

Figure 5.12: Force in the slip direction acting on plane $x = 0$ at time instant $t = 6.0$.

reason why stresses seem to fade out on the right half of figures. All figures show, that introduction of an edge in fault geometry results in generation of additional stresses in close neighborhood of the edge. Presented snapshots of normal stress are plotted at a time when the whole rupturing process has already developed.

Next setting we had studied was exactly the same as already discussed, except that the nucleation point of the rupturing process was shifted into point $N = (0.0, -0.5, 0.0)$. Rupture front propagates with the same velocity $v_r = 3$. We were motivated by the belief that the arrival of rupture front to the edge of planar part of the fault should have some effect on the resulting wave field. We present snapshots of first velocity component in the plane $z = 0$, which is perpedicular to the fault zone and intersects the fault right in the center. Figures 5.14, 5.15 show snapshots for two source geometries – the first is planar and labeled by $\boldsymbol{n}_2^0$, the second one labeled $\boldsymbol{n}_2^2$ - recall (5.5.3).

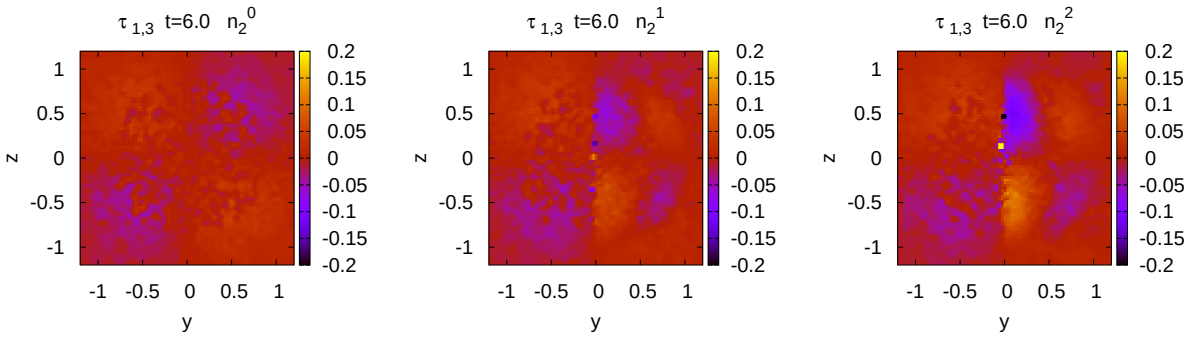

Figure 5.13: Fault tangent slip-perpendicular force acting on plane $x = 0$.

There are noticeable changes in the wave field. The most apparent change in two fields is that the direction in which the fault radiates with biggest amplitude changes accordingly to changes in the fault geometry. Figure 5.16 presents the difference of two wave fields presented in figures 5.14 and 5.14. The figure suggests that the arrival of the rupture to the edge actually produces a disturbance in the wave field which propagates from the edge.

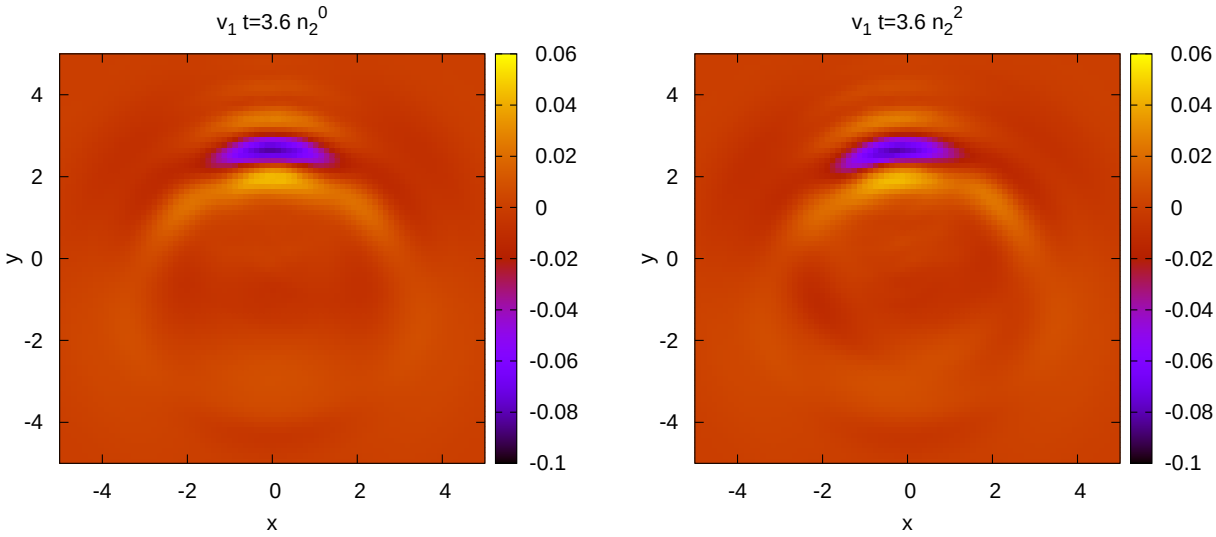

Figure 5.14: Snapshots of first velocity component at time $t = 3.6$ for two source geometries.

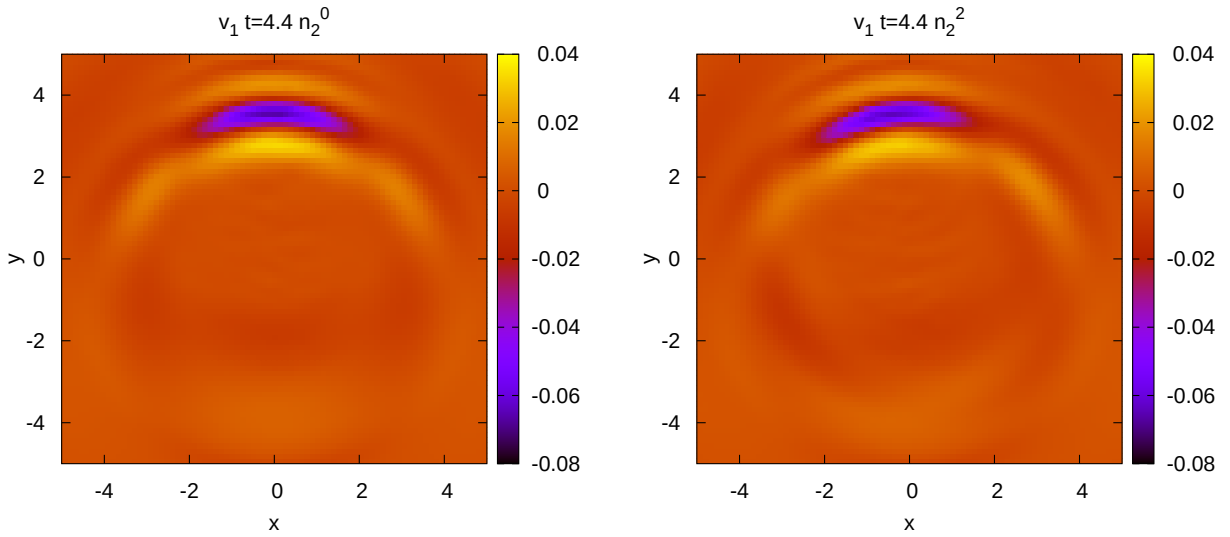

Figure 5.15: Snapshots of first velocity component at time $t = 4.4$ for two source geometries.

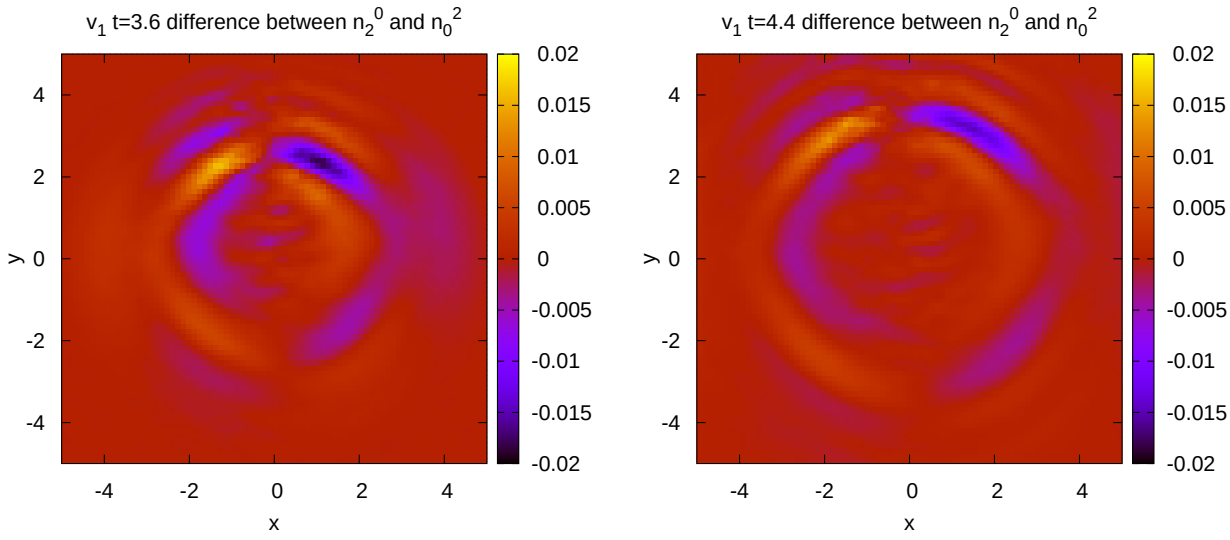

Figure 5.16: Difference of first components of velocities for two time instants $t = 3.6$ and $t = 4.4$. Two velocity fields were computed for geometries labeled as $\boldsymbol{n}_2^0$ and $\boldsymbol{n}_2^2$.

Chapter 6

Summary

Whole work was aimed at numerical methods for obtaining an approximate solution for various settings of problems. Relevance of kinematic models greatly depends on physical sense for the problem of the one who designs them.

Although mathematical formulation of the problem seems straightforward, there are several issues concerning creation of discontinuity that deserve a closer look. Weak formulation of the problem is identical to one already used by Tomáš Pergler in his master thesis [15]. We did not show exact proof of existence and uniqueness, because it can be easily obtained from given references. Neither we have shown the independence of result on the choice of slip function extension. This assertion can be shown very similarly to the case of non-zero Dirichlet boundary conditions.

Results presented in the work were computed on a 3GHz, 3Gb RAM personal computer. Thanks to contemporary computers, we were able to compute problems with up to approximately 700 000 degrees of freedom. However, this often was not sufficient to reduce spurious oscillations in our results. When we compared outcomes of our computations with data obtained by another numerical methods, we found that our results contain artificial oscillations. These artificial oscillations are believed to be generated by poor spatial resolution [5]. Literature offers several algorithms for time-integration that exhibit artificial damping to reduce these spurious oscillations. We have presented two algorithms for time-integration. One which does not dissipate and one that does. After several tests made, we found that two algorithms give the same results, so only Bossak's algorithm was used for all computations. For most of computations we had used algorithm with such parameters which assured no dissipation.

We have attempted to study spectra of seismograms and their dependence on spatial resolution of mesh. Receivers for which seismograms were

recorded were situated very close to the source fault. Our results show, that quite narrow band of frequencies was affected by the resolution variance. We believe that sufficient spatial resolution will give results with small spurious oscillations pollution.

In the last section we have studied effects of nonplanar source geometry. We have made computations for several cases of piecewise planar fault, varying in the angle made by two parts of fault surface. We presented figures of a normal stress on the fault surface. Results for normal stresses on the fault zone show, that introduction of an edge in geometry generates additional stresses close to the edge. We have also studied a velocity field. We have presented figures which show that the wave field is significantly altered by geometry of the fault. Difference of two velocity fields computed for two geometries indicates that arrival of rupture front to the edge of geometry generates a disturbance which then propagates from the edge.

It has become obvious, that proposed numerical method is not suitable for simulation of long distance wave propagation, but rather for evaluation of displacements or stresses very close to the source, where also finite dimensions of source can be appreciated in resulting approximate solution.

Appendix A

Important theorems

Theorem A.0.1. *(TRACE THEOREM) Assume Ω is bounded and $\partial\Omega$ is C^1. Then there exists a bounded linear operator*

$$T : W^{1,p}(\Omega) \to L^p(\partial\Omega)$$

such that

- $Tu = u|_{\partial\Omega}$ *if* $u \in W^{1,p}(\Omega) \cap C(\overline{\Omega})$
- *and*

$$||Tu||_{L^p(\partial\Omega)} \leq C\,||u||_{W^{1,p}(\Omega)}$$

for each $u \in W^{1,p}(\Omega)$, with the constant C depending only on p and Ω. Tu is called the trace of u on $\partial\Omega$.

Theorem A.0.2. *(KORN'S INEQUALITY) Let Ω be a bounded region, with $\partial\Omega = \Gamma_D \cup \Gamma_N$. $\Gamma_D \cap \Gamma_N = \emptyset$. Let $V \equiv \{\boldsymbol{v} \in W^{1,2}(\Omega;\mathbb{R}^3) : \boldsymbol{v}|_{\Gamma_D} = 0\}$. Let Γ_D have positive two dimesional measure. Then*

$$\int_\Omega \boldsymbol{\varepsilon}(\boldsymbol{v}) : \boldsymbol{\varepsilon}(\boldsymbol{v}) \geq ||\boldsymbol{v}||_{W^{1,2}(\Omega;\mathbb{R}^3)} \qquad \forall \boldsymbol{v} \in V \tag{A.0.1}$$

Proof. Proof of this statement can be found in [13]. □

Bibliography

[1] Fftw. A library for FFT computations www.fftw.org.

[2] Netgen 4.4 a tetrahedral mesh generator - http://www.hpfem.jku.at/netgen/.

[3] Sparselib++. C++ class library for efficient sparse matrix computations. http://math.nist.gov/sparselib++/.

[4] D.J. Andrews. Evaluation of static stress on a fault plane from a green's function. *Bulletin of Seismological society of America*, 1974.

[5] J. Chung and G. M. Hulbert. A time integration algorithm for structural dynamics with improved numerical dissipation: the generalized-α method. *Journal of Applied Mechanics*, 60:371–375, 1993.

[6] Vitásek Emil. *Numerické metody.* SNTL, Prague, 1987.

[7] Patrick Keast. Moderate degree tetrahedral quadrature formulas. *Computer Methods in Applied Mechanics and Engineering*, 55:pages 339–348, 1986.

[8] Peter Knabner and Lutz Angermann. *Numerical methods for elliptic and parabolic partial differencial equations.* Springer, 2003.

[9] J. B. Lambert. *Computational Methods in Ordinary Differential Equations.* London : Wiley, 1973.

[10] Evans L.C. *Partial differential equations.* AMS, 1997.

[11] R. Madariaga. *Eartquake source theory: a review, in: Earthquakes: Observation theory and interpretation.* North-Holland, 1983.

[12] Brdička Miroslav. *Mechanika kontinua.* ČSAV, 1959.

[13] Jindřich Nečas and Ivan Hlaváček. *Úvod do matematické teorie pružných a pružně plastických těles.* Prague SNTL, 1983.

[14] N. M. Newmark. A method of computation for structural dynamics. *Proc. A.S.C.E.*, 1959.

[15] T. Pergler. Postseismic relaxation of the earth's models described by maxwell rheology (in czech). Master's thesis, Faculty of mathematics and physics, Charles university, Prague, 2004.

[16] T. Roubíček and M. Kružík. Mathematical methods in continuum mechanics of solids. lecture notes, in preparation, 2007.

[17] O.C. Zienkiewicz, M. Bossak, and W.L. Wood. An alpha modification of newmark's method. *International Journal for Numerical Methods in Engineering*, 1980.

[18] O.C. Zienkiewicz and O.C. Taylor. *The finite element method. Fith edition. Volume 1 - The basis.* Butterworth-Heinemann, 2000.